# Improving the Performance of the CMS ECAL Trigger Energy Reconstruction Algorithms for LHC Run 3

William Richard Smith

School of Physics and Astronomy,
University of Southampton

*Supervisor*
David A. Petyt

In partial fulfillment of the requirements for
the degree of Master of Physics and Particle Physics

May 9, 2019

# Abstract

The CMS electromagnetic calorimeter (ECAL) is a high-resolution crystal calorimeter that provides precise measurements of the energies of electrons and photons at the CERN LHC. A fast energy reconstruction algorithm is implemented in the on-detector electronics, which is based on a digital filtering method and weighted signal sum. This provides energy sums to the trigger system of CMS, which determines whether an event is interesting enough to be written to disk. Despite the challenges of an ageing detector, higher luminosities and increasing pileup, it is vital that the best trigger performance is maintained for LHC Run 3 (2021-23) physics analyses. The current performance of the ECAL trigger algorithm was evaluated using CMS event data from LHC Run 2 (2015-18). An updated set of signal weights, that better suit Run 2 detector conditions, was produced and yielded improved energy reconstruction. More granular weights were investigated and were found to further improve the energy reconstruction performance. Finally, weights optimised for different levels of pileup were computed and were found to significantly reduce the energy bias and its dependence on eta ring, position within the LHC bunch train and energy level. In all cases studied here, updated weights were an improvement over the current weights and as the PU level at the LHC increases, the use of PU optimised weights will become even more vital for accurate energy reconstruction within the ECAL to ensure a high trigger efficiency for physics signatures.

# Acknowledgements

I would like to thank my supervisor Dr David Petyt for his help, guidance and insight throughout the past year. In addition, I would like to thank the course coordinator Prof. Stefano Moretti, the University of Southampton, and the Rutherford Appleton Laboratory, for arranging this course and giving me the opportunity to spend the year working at CERN.

# Contents

# 1 Introduction

The Large Hadron Collider (LHC) at CERN, Geneva is the largest and most powerful particle accelerator in the world. Built to investigate predictions from the standard model and search for new physics, the LHC collides protons at a centre of mass energy of 13 TeV. Two beams containing up to 2808 proton bunches are accelerated in opposite directions around the 26.7 km ring at speeds approaching the speed of light. The beams are then made to collide in four different detectors [1], each designed to investigate a wide range of physics. One such general-purpose detector at CERN is the Compact Muon Solenoid (CMS) [2].

In July 2012, the CMS and ATLAS Collaborations independently discovered the existence of the last fundamental particle predicted by the standard model: the Higgs Boson [3], thereby confirming the theory of spontaneous electroweak symmetry breaking as the method by which W and Z bosons acquire mass. In CMS, the discovery was reliant on the detector having high sensitivity to the Higgs decay channels, $\mathrm{H} \to \gamma\ \gamma$ and $\mathrm{H} \to \mathrm{ZZ}^* \to 4l$. The photons and electrons produced in these decays are measured by the electromagnetic calorimeter (ECAL), which has been designed to have the highest energy resolution possible. It is vital for future physics discoveries that this performance is maintained.

The ECAL uses algorithms to precisely measure the energy of photons and electrons from CMS data, in order to identify potentially interesting events and trigger on them. These algorithms must be fast and accurate to cope with the LHC collision rate of 40 MHz, especially as the LHC enters its third data run in 2021 (Run 3), where greater luminosity levels will be reached. The principal algorithm is based on a digital filtering method that uses a weighted signal sum to determine the overall energy of a particle. To maintain the best possible ECAL performance, the energy reconstruction algorithm must continue to work efficiently and accurately, despite the challenges of an ageing detector, increasing luminosity and changing beam conditions. Optimising this algorithm by updating the weights used in the weighted sum to better suit current and future detector and beam conditions forms the focus of this project.

This report is organised as follows. Firstly, the CMS detector is introduced and the elements of the ECAL are described. The functionality of the CMS trigger system, which selects interesting events from the LHC collisions is summarised, and the energy reconstruction algorithm used in the ECAL trigger is described in detail. The challenges posed by the harsh LHC radiation environment, increased luminosity and changing beam conditions are outlined and the impact on the performance of the current ECAL trigger algorithms is evaluated. Various improvements are investigated, including deriving more optimal amplitude reconstruction weights from recent CMS data, as well as investigating more granular weights that better account for the radiation-dependent effects in different regions of the detector. Finally, a summary of the next steps in the project will be outlined, which involve new methods that should further improve the ECAL trigger performance in the future.

# 2 CMS

CMS comprises a series of concentric cylindrical layers, each designed to provide information about the different particles produced in the proton-proton collisions. Closest to the interaction point, the tracker determines a particle's momentum by measuring its trajectory in a strong magnetic field. The path of a charged particle can be used to reconstruct the interaction vertices [4]. Surrounding the tracker is the ECAL, which will be described in further detail below. The hadron calorimeter (HCAL) makes up the next layer, where hadron energies are measured [5]. After the 3.8 T superconducting magnet, the muon detector forms the outermost layer [6]. A cross-section of the inner regions of CMS is shown in Figure 1.

## 2.1 ECAL

The ECAL is a crystal calorimeter, as shown in Figure 2, comprising a barrel (EB) covering the pseudorapidity range $0 \leq |\eta| \leq 1.479$ and two endcaps (EE+ and EE-) covering the range $1.479 < |\eta| \leq 3.0$. EB contains 61,200 lead tungstate crystals and EE (EE+ and EE-) contains 14,648. For triggering purposes, these crystals are organised into eta rings, as shown in blue in Figure 1.

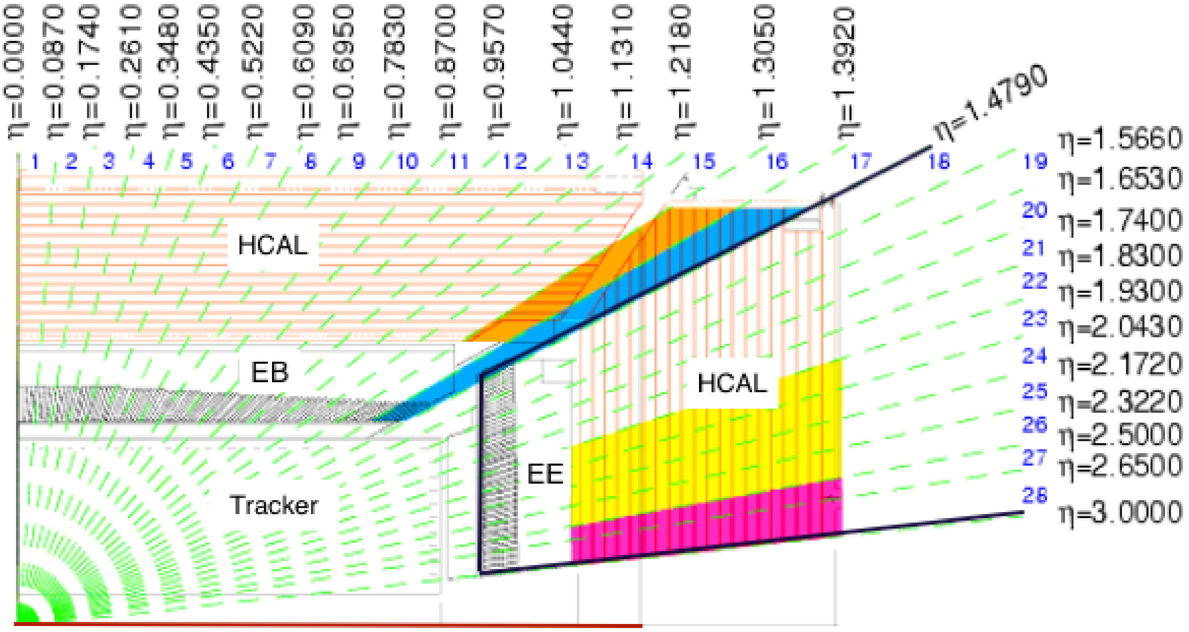

Figure 1: Upper quadrant of the long axis cross-section of CMS, showing the tracker, the ECAL Barrel (EB) and Endcaps (EE) and the HCAL. The numbered rings of pseudorapidity are labelled in blue, with their corresponding eta range. EE+(-) comprises rings (-)18 to (-)28 and EB comprises rings -17 to +17. The red line represents the beam axis. Figure from [7].

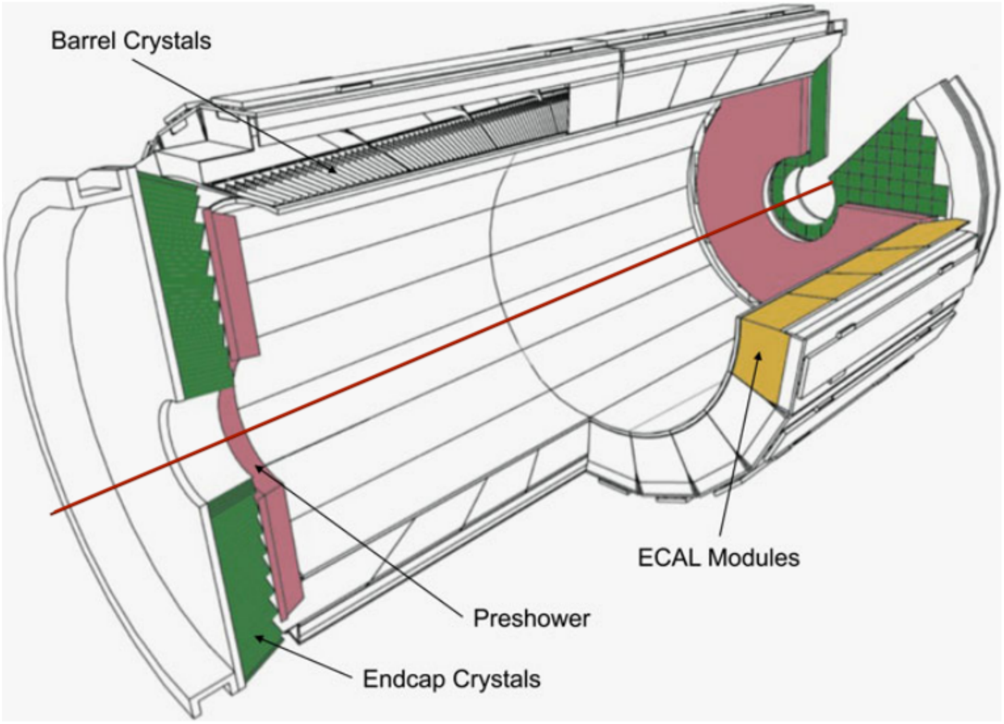

Figure 2: Schematic diagram of ECAL, showing the Barrel, Endcaps and Silicon Preshower. The red line represents the beam axis. Figure from [8].

When an electron or photon interacts with an ECAL crystal it loses energy and an electromagnetic shower begins. High energy electrons primarily lose energy through Bremsstrahlung radiation, where they are decelerated from the deflection off lead tungstate nuclei within the crystals, producing high energy photons. These high energy photons, or indeed the photons created directly in the initial proton collision, then convert into electron-positron pairs. This process continues until the shower has lost enough energy to ionise the scintillation crystals, whereupon light is emitted with a peak wavelength of 420 nm. This light is measured by Avalanche Photodiodes (APDs) in the barrel and by Vacuum Phototriodes (VPTs) in the endcaps [9].

## 2.2 CMS Trigger System

In 2017, the luminosity of the LHC colliding beams reached $2.06 \times 10^{-34}\,\mathrm{cm}^{-2}\,\mathrm{s}^{-1}$, producing approximately one billion proton interactions per second. This much data cannot possibly be stored on disk, and so a system which only triggers on interesting physics events is required [10]. This real-time event selection is performed by the CMS trigger system, which comprises two levels. The Level-1 (L1) trigger takes place in custom hardware on-detector and reduces the trigger rate to a maximum of 100 kHz, whereas the high-level trigger (HLT) is software-based and is executed on a farm of 13,000 commercial CPUs, further reducing the rate to around 1 kHz. The bandwidth of the 100 kHz L1 Trigger rate is shared amongst the different physics analysis groups, and the specific allocation is designed to allow for the broadest range of analyses to be carried out. An example bandwidth allocation for 2017 can be seen in Figure 3.

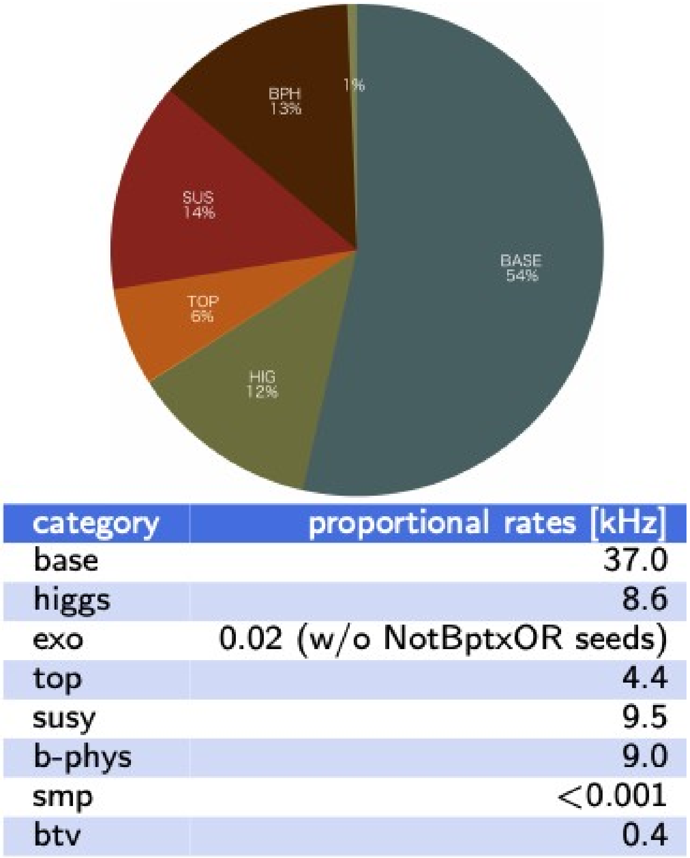

| category | proportional rates [kHz] |
|---|---|
| base | 37.0 |
| higgs | 8.6 |
| exo | 0.02 (w/o NotBptxOR seeds) |
| top | 4.4 |
| susy | 9.5 |
| b-phys | 9.0 |
| smp | <0.001 |
| btv | 0.4 |

Figure 3: L1 Trigger bandwidth allocation for different physics analysis groups. ‘Base’ refers to general purpose triggers such as single electron, single muon, single tau or single jet, that are not specific to any one analysis. Data from 2017 Fill 6358. Figure from [11].

### 2.2.1 Level-1 Trigger

The L1 Calorimeter Trigger is designed to identify photons, electrons, jets, muons and missing transverse energy with a very high efficiency in different regions of the detector and above certain energy thresholds. These objects are used in the search for new physics. For example, in supersymmetry, a postulated light and weakly interacting particle carries energy away from the LHC collisions without interacting with the detector. The energy from low energy events is summed, and the missing energy, which has been transferred to the postulated supersymmetric particles, is calculated. At the higher energy scale, single electron or photon triggers, around 30 GeV, form the basis of many general physics searches, particularly Z, W and Higgs decays. Jets, which can contain a mixture of photons, charged and neutral hadrons, are produced in many processes and give information about QCD events and rare decays. Further areas of new physics include W-W boson scattering, beyond-standard-model Z' bosons and top quark decay [12].

The LHC collision frequency of 40 MHz results in protons entering the detector every 25 ns, which is faster than the detector can process an event. The L1 trigger therefore has a latency of 3.2 µs to store event data, during which time it must decide whether to accept or reject an event using information provided by the different subdetectors. The calorimeter trigger receives transverse energy sums from the ECAL and HCAL and forms electron, photon or jet candidates. This is combined with further identification information from the global muon trigger in the global trigger, which then makes the final accept/reject decision based on the presence of physics objects, such as photons, electrons, muons, jets and missing energy. If present, the identified physics object must surpass a pre-determined energy threshold for the event to be accepted. Upon receipt of an L1 accept decision, the CMS data acquisition system will read out the data from the subsystems corresponding to the accepted event. This data is further processed by the HLT, where the filtered events are written to permanent storage for analysis [13].

Improving the performance of the energy reconstruction algorithms within the ECAL L1 Trigger has important and beneficial consequences for the search for physics. If the energy reconstruction is no longer accurate, the energy measurements of physics objects will be biased and the resolution will be poor. With a positive energy reconstruction bias, the measured energy of some events will be overestimated and increased above the energy threshold for read-out, resulting in an unnecessary trigger and an increased trigger rate. But the maximum rate of the L1 trigger is fixed, so the energy threshold must be increased to reduce the rate to an acceptable level, reducing efficiency for physics signatures and wasting valuable physics events. Conversely, a negative energy reconstruction bias results in an underestimate in the energy measurement, reducing the energy of a potentially interesting physics event below the threshold such that the event is lost.

### 2.2.2 ECAL Trigger Primitives

The online transverse energy sums sent from the ECAL are called trigger primitives (TPs), and are generated on-detector in real-time. They provide estimates of the energy and time of electromagnetic signals summed over several crystals. Due to the high LHC collision rate, these are fast energy sums calculated using a simple algorithm. It is crucial for detector performance and trigger efficiency that the TPs are accurate despite this.

The TP generation starts in an APD/VPT, which converts the scintillation light from electron or photon showers in a crystal into an analogue electrical signal. Five of these photodetectors then read out to one very-front-end card (VFE), where the electrical signal for each channel is shaped and amplified by a multi-gain preamplifier (three gain levels) and digitised by a 12-bit analogue-to-digital converter with a 25 ns sampling rate. One front-end card (FE) then receives the digitised signals from five VFE cards, whereupon each signal is linearised in a FENIX chip [14]. This process involves applying calibration constants to calculate the transverse energy deposited in the crystal. These five linear signals are then sent to a sixth FENIX chip, which sums them into one signal for the 5x1 crystal strip. The amplitude of the strip signal is proportional to the total energy deposited in the strip. Next, a digital filter is applied to find the maximum signal amplitude. This filter comprises five weights that multiply the signal at 25 ns time intervals. This will be discussed in further detail in section 2.2.3. Finally, a peak finder is applied to determine the LHC bunch crossing where the maximum signal occurs. This process is summarised in Figure 4.

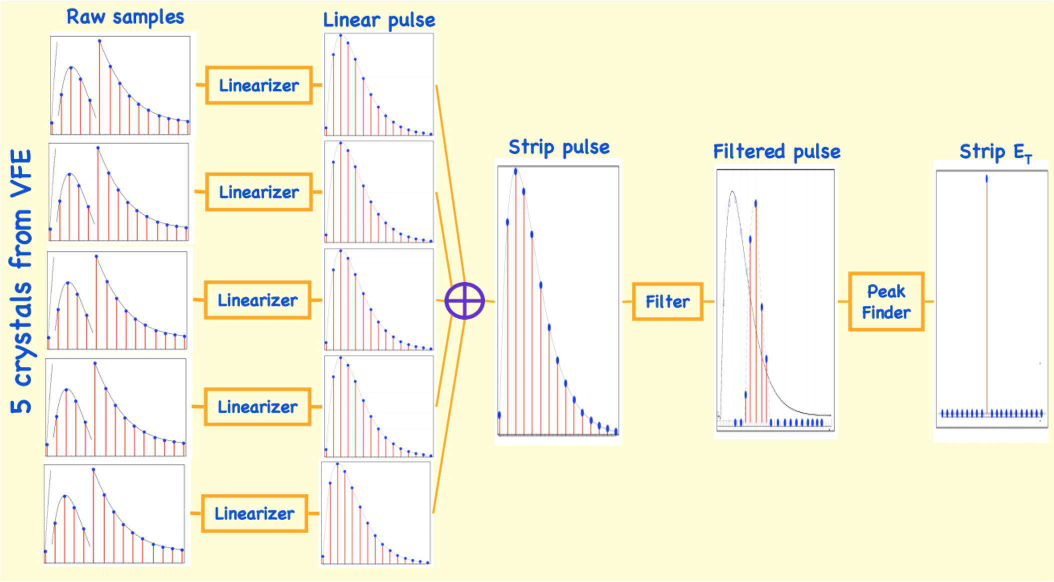

Figure 4: TP generation algorithm that takes place on the FE card. Figure from [11].

### 2.2.3 Weights Digital Filter

The estimation of the signal amplitude is performed by a digital filter, which involves multiplying the strip signal at 25 ns time intervals by a weighting factor, as seen in Figure 5:

$$\hat{A} = \sum_{i=1}^{n} S_i w_i \quad , \tag{1}$$

where $\hat{A}$ is the signal amplitude estimator, $S_i$ is the signal value at time sample $i$, $w_i$ is the corresponding weighting factor and $n$ is the total number of signal samples/weights.

The amplitude estimator must be unbiased and equal to the true amplitude, which leads to the following conditions:

$$\sum_{i=1}^{n} w_i f_i = 1 \quad \text{and} \quad \sum_{i=1}^{n} w_i = 0 \quad , \tag{2}$$

where $f_i$ is the value of a template pulse, $f(t)$, at time $i$. The template pulse is an analytic function [15] that describes the expected shape of a signal pulse, shown in Figure 6, as measured in an electron test beam:

$$f(t) = (1 + \frac{(t - T_{max})}{\alpha\beta})^{\alpha} e^{-a(\frac{t - T_{max}}{\beta})} \quad , \tag{3}$$

where $\alpha$ and $\beta$ are pulse shape parameters, with separate parameters for EE and EB.

The weights are calculated by minimising the variance in the amplitude estimator when the weights are applied to the template pulse [16]. The simplest method to reconstruct the maximum signal amplitude would be to take a single measurement at the signal maximum. This corresponds to having one weight with unit value, which multiplies the signal at its peak. Although fast, this method does not allow for the subtraction of a noise pedestal offset or pileup (PU) effects, which is when signals originating from different LHC bunch crossings overlap in the same crystal. Additionally, with more than one weight, a significant reduction in the noise is possible. Five weights are currently used in the digital filter, giving a 40% noise reduction compared to one weight [17]. Two different sets of weights, one for EE and one for EB, have been used unchanged in the ECAL FE cards since CMS started taking data in 2008 and are listed below in Table 1.

|  | w1 | w2 | w3 | w4 | w5 |
|---|---|---|---|---|---|
| EE | -0.656250 | -0.515625 | 0.250000 | 0.515625 | 0.406250 |
| EB | -0.562500 | -0.546875 | 0.250000 | 0.484375 | 0.375000 |

Table 1: Current EE and EB weights.

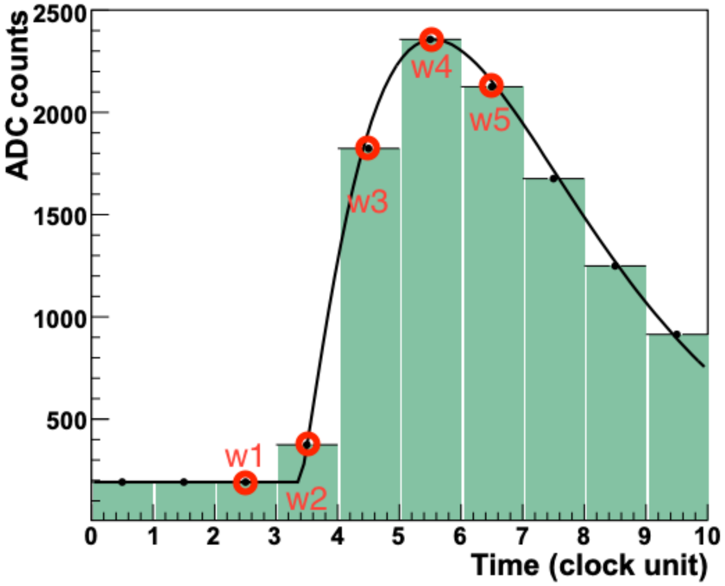

Figure 5: Example digitised signal pulse. One clock unit equals 25 ns. Each weight multiplies the signal at the corresponding red dot, i.e. at 50, 75, 100, 125 and 150 ns respectively.

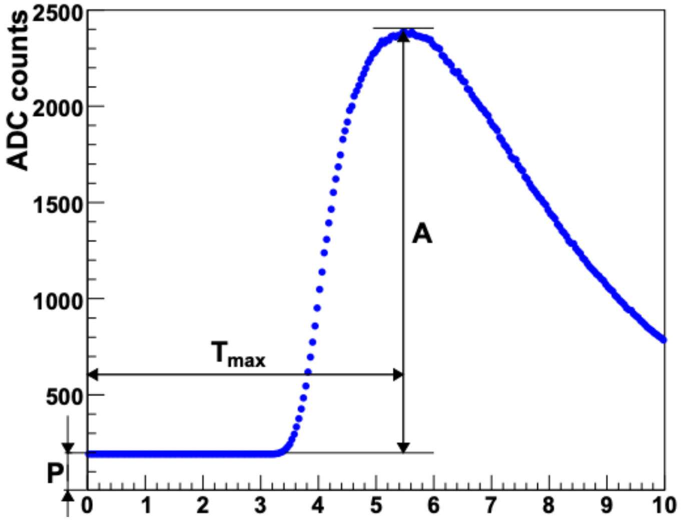

Figure 6: The template pulse $f(t)$, where P represents the noise pedestal, $\mathrm{T}_{\mathrm{max}}$ represents the time at the maximum signal amplitude and A represents the maximum signal amplitude. Figure from [18].

# 3 Project Rationale

## 3.1 Crystal Damage and Pulse Shape Change

Since the weights were first calculated and the LHC switched on for data-taking in 2008, much has changed. The detector has aged significantly and the crystals have been heavily irradiated by the high luminosities, causing permanent darkening. Two main mechanisms contribute to this darkening and crystal transparency loss. The first is the formation of colour centres, caused by ionising radiation displacing anions within the crystal lattice, which then get filled with unpaired electrons and absorb light. The second mechanism comes from the direct collision of high energy hadrons with the nuclei in the crystal lattice. The nuclei split into charged fragments and propagate through the crystal, ionising other nuclei within the crystal and creating permanent colour centres [19]. Laser light is injected into the ECAL crystals to constantly monitor this damage and correct for the loss in light response. Figure 7 shows the significant degradation in the response across different eta regions, especially in eta ring 28 ($|\eta| > 2.7$), where the response has changed by 90%. A laser correction (LC) multiplier is applied to counteract this.

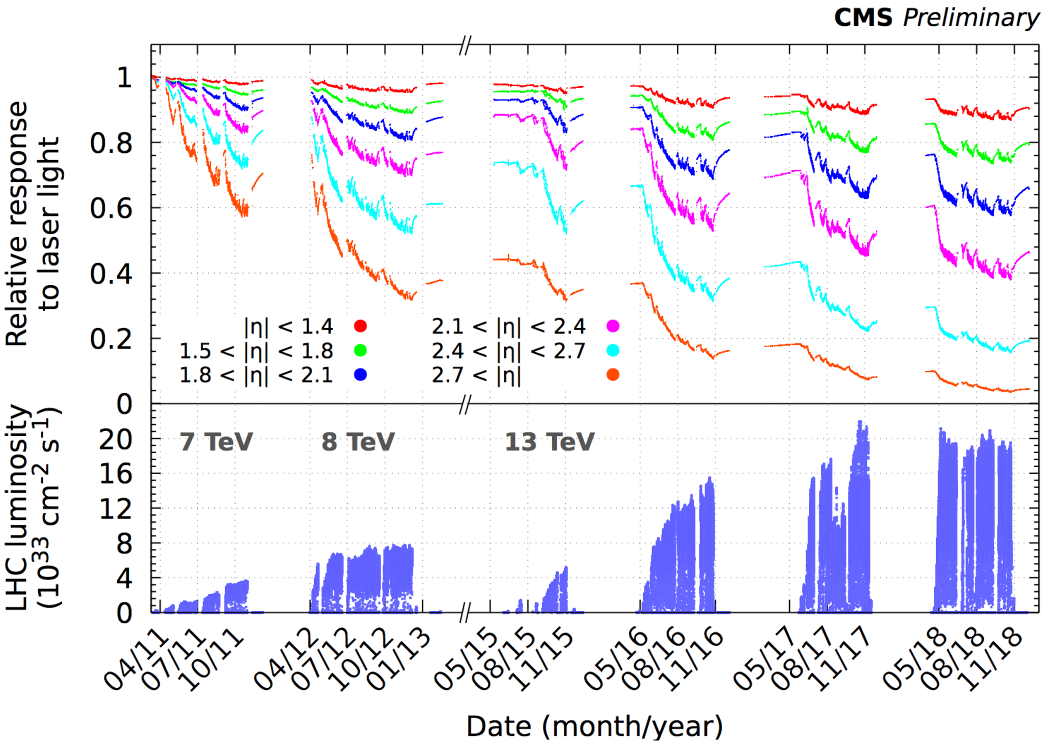

Figure 7: Relative response to laser light in the ECAL crystals, measured by the ECAL laser monitoring system, averaged over all crystals in bins of pseudorapidity, for the 2011, 2012 and 2015-18 data-taking periods. The bottom plot shows the instantaneous LHC luminosity delivered during these time periods. Figure from [20].

Damaged crystals respond differently to undamaged crystals. The reduced light path length in damaged crystals results in pulse shapes that are significantly different to the original template pulse (Figure 6). Figure 8 shows how the pulse shape varies with LC, where a larger LC means a more damaged crystal. If a crystal pulse shape differs from the template pulse used to originally calculate the weights, the accuracy of the signal amplitude reconstruction will be reduced.

Not only has the average pulse shape changed over time, but the effective signal noise has increased too. Although the LC corrects the loss in response, it also multiplies any noise within the crystal. Current LCs within eta ring 28 were approximately 20-30 in August 2018, giving a substantial noise amplification factor.

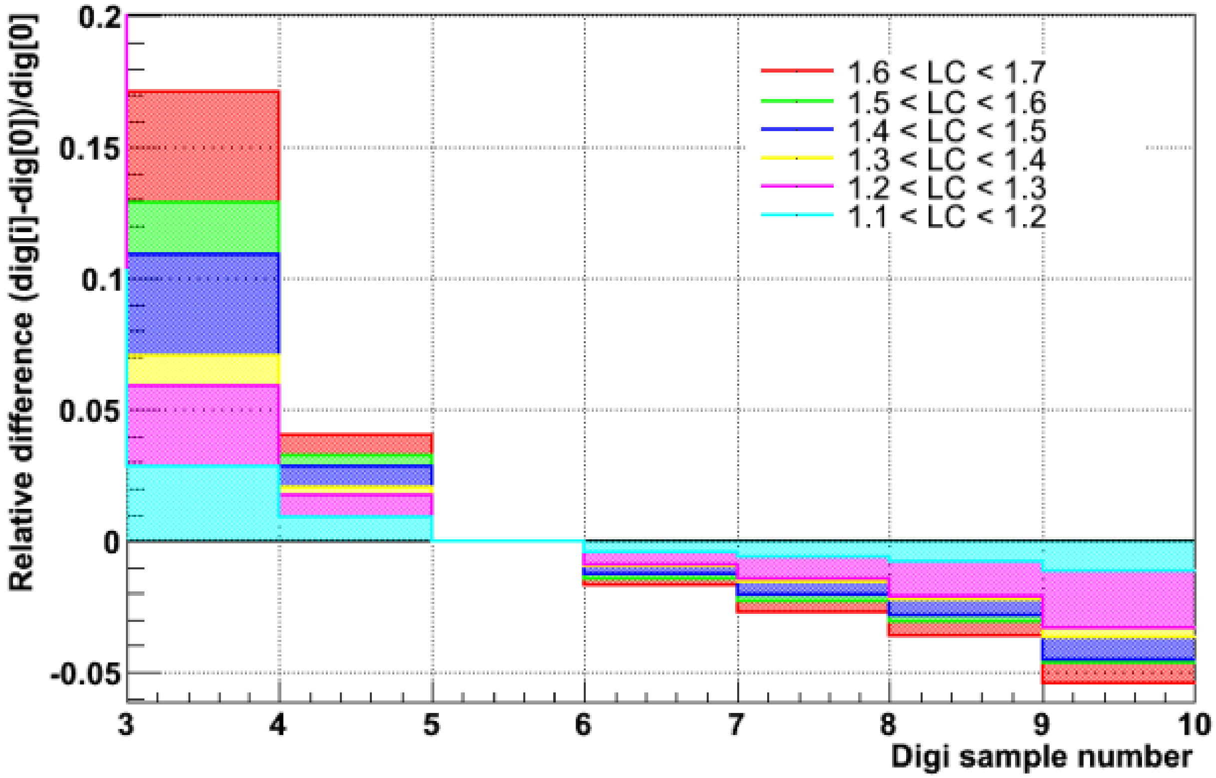

Figure 8: The variation of ECAL endcap pulse shapes as a function of laser correction factor, LC, which multiplies the signal in a crystal to counteract any loss in response caused by radiation damage. The pulses are aligned about the signal maximum (bin 5). The pulse shapes in more damaged crystals rise earlier and fall faster than in undamaged crystals. Figure from [21].

### 3.2 Increased Pileup

The number of proton-proton collisions occurring at each LHC bunch crossing is known as pileup (PU). The PU evolves over time with the luminosity during an LHC fill, with a typical peak PU of 55 in 2018. At high luminosities and large PU, signals from multiple bunch crossings overlap in the same crystal, as shown in Figure 9. The signals constructively interfere, such that the observed signal contains contributions from multiple pulses and different bunch crossings. This is problematic, as the observed final energy of a collision will actually be a combination of the in-time signal and products from other pileup events, making the energy reconstruction of jets, missing energy, electrons and photons less accurate. These objects form the basis of many physics analyses, and so any reconstruction bias is a concern [22].

Higher levels of PU can artificially increase the measured energy of a physics object, increasing the rates for different physics triggers, sometimes uncontrollably. As seen in Figure 10, the missing energy trigger rate does not scale linearly with PU. Instead, at PU 50 the rate increases dramatically, requiring an increase in the energy threshold to reduce the rate back to an acceptable level. As a result, fewer events are recorded and potentially interesting physics is lost.

As the luminosity of the LHC has been increasing, so too have the PU levels. Indeed, LHC Run 3 is likely to see unprecedented levels of the two, and without improved and optimised algorithms to mitigate the negative effects of PU, the increased number of collisions will not be fully utilised for physics.

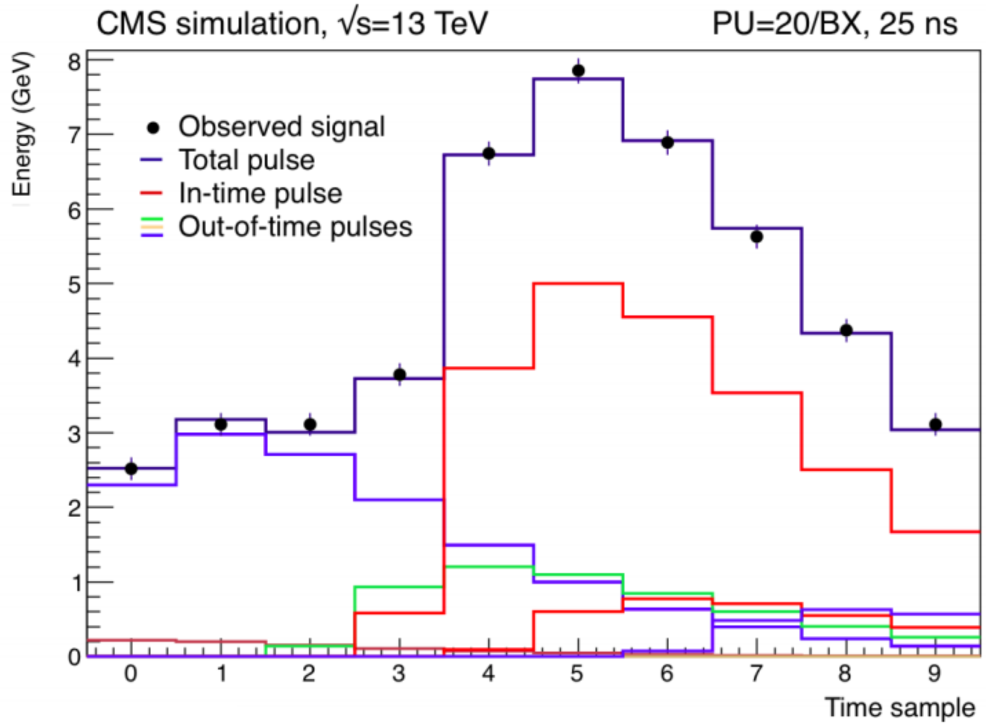

Figure 9: Example of multiple signals overlapping in the same crystal at PU = 20. The out-of-time pulses are shown, and the impact on the in-time pulse can be seen. Figure from [23].

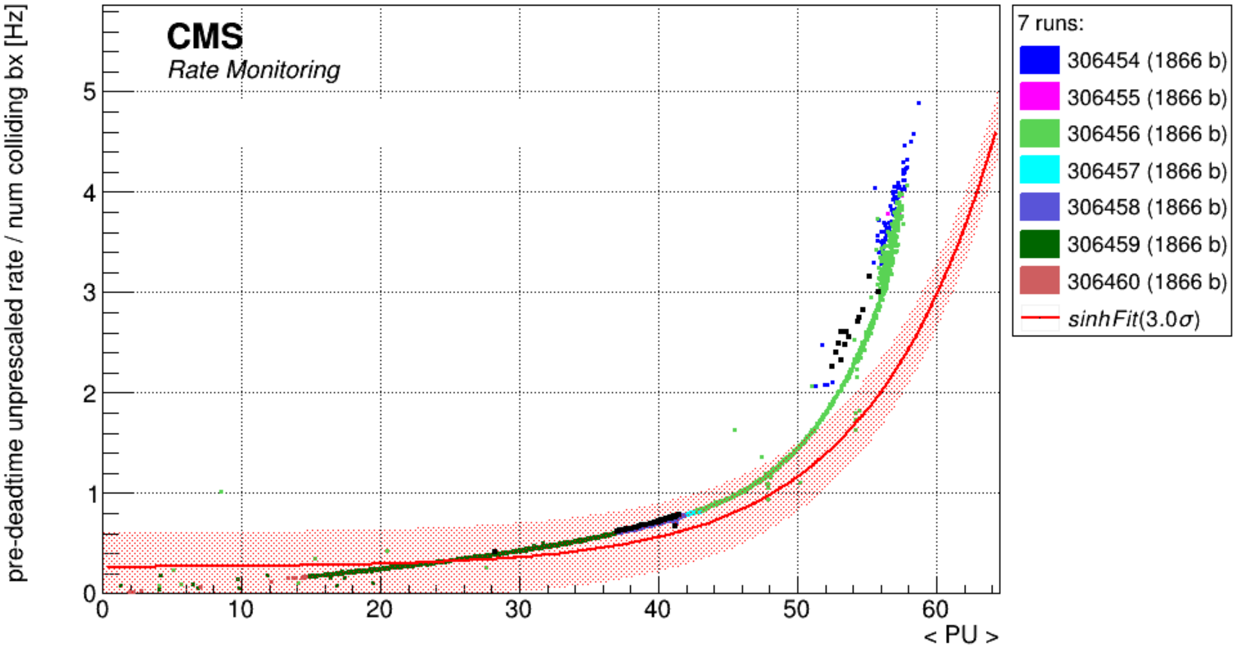

Figure 10: Rate vs PU for the missing energy trigger. The rate increases significantly above PU 50. The red fit is from earlier 2017 data. Figure from CMS Web Based Monitoring rate plots.

## 3.3 LHC Filling Schemes

The LHC beam contains 3564 radio frequency buckets, which can either be empty or filled with a proton bunch. The configuration of this bunch train, known as the bunch filling scheme, has strong implications for the LHC luminosity level, beam dynamics, experimental operation and detector performance [24].

Since 4 separate detectors, requiring different beam characteristics, share the same beam, the bunch filling scheme has to be carefully chosen to optimise certain properties. For CMS, the highest possible luminosity is desirable to maximise the number of collisions. Towards the end of 2017, a filling scheme called 8b4e was adopted, an example of which is seen in Figure 11. Eight consecutive proton bunches are followed by four empty bunches, and this pattern repeats throughout the bunch train. This filling scheme suppresses the formation of electron clouds and reduces the heat load on the quadrupole magnets, resulting in a more sustainable beam, albeit with large variations in the out-of-time PU contribution. Because of this, 8b4e proved challenging for the ECAL L1 Trigger, with higher trigger rates, lower efficiency and a strong bunch position dependence. As seen in Figure 12, most events come from positions two and three of the 8 bunches, most likely due to a large energy reconstruction bias in the TPs.

In 2018, the LHC changed filling schemes back to 48b, which comprises forty-eight consecutively filled proton bunches, followed by a gap of at least seven bunches, as seen in Figure 13. With the longer bunch train, out-of-time PU levels are more stable for the majority of the bunch positions, resulting in more predictable L1 Trigger performance. For LHC Run 3, starting in 2021, discussions are ongoing as to which bunch filling scheme should be used. 8b4e, 48b or a combination of the two have been suggested, and so it is vital the effects of these schemes on detector performance, specifically the Trigger Primitives, is understood. As seen in Figure 14, which uses data from a special test fill with large PU levels and both 48b and 8b4e bunch trains, the rates of both filling schemes behave predictably up to PU 55, remaining below the 100 kHz maximum L1 Trigger rate. Beyond that, the rates increase rapidly and quite differently. A mixed scheme could combine the benefits of the two filling schemes whilst reducing the negative effects of 8b4e. Therefore, studies will be carried out on both 8b4e 2017 and 48b 2018 data to understand the bunch position dependencies present and investigate the possible improvements updating the weights and increasing the weight granularity has on the robustness of the TPs to out-of-time PU.

## 3.4 Summary

In summary, the crystals have been damaged by the LHC beams, especially in high eta regions, causing shifts in the average pulse shapes and an increase in the signal noise. PU levels have increased, reducing the accuracy of the energy measurements of physics objects, resulting in a higher trigger rate, requiring an increase in the energy threshold and a decrease in the number of events being recorded. Furthermore, the consequences of changing bunch train filling scheme needs to be fully understood. It is possible that updated or more granular weights could reduce the PU and bunch position dependence of the energy reconstruction, providing significant performance improvements.

The method and results are presented in the following sections. First, the performance of the current weights on 2018 CMS data will be studied. The possibility of updating them to better suit current detector conditions will follow, before a detailed investigation into the benefits of more granular weights and weights optimised for specific levels of PU.

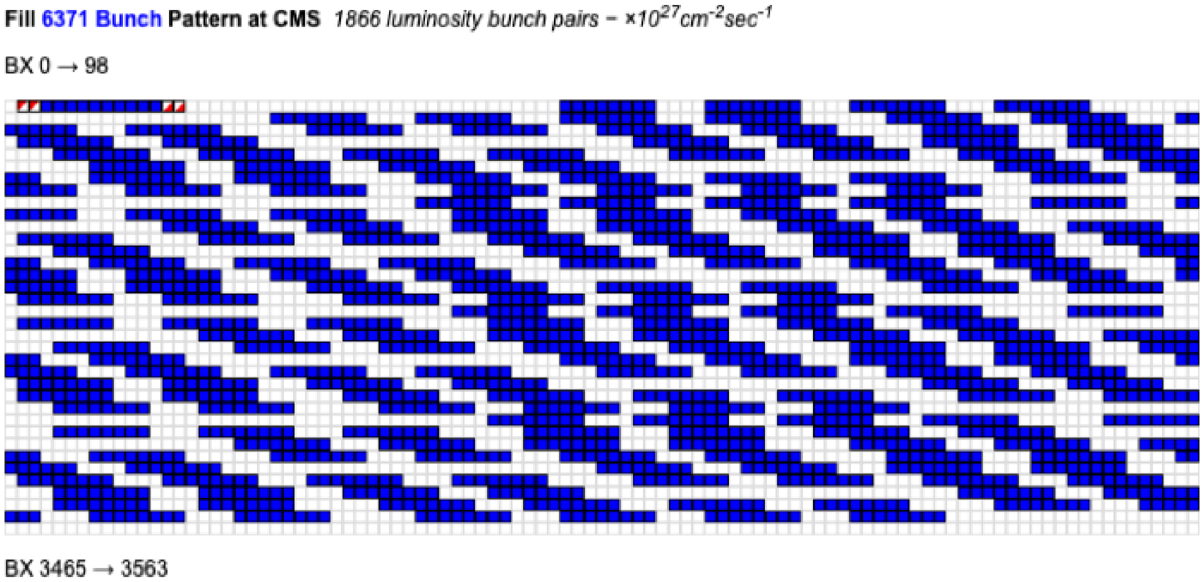

Figure 11: Example of an 8b4e bunch filling scheme from Fill 6371, recorded in November 2017. The blue boxes indicate a proton bunch. Figure from CMS Web Based Monitoring.

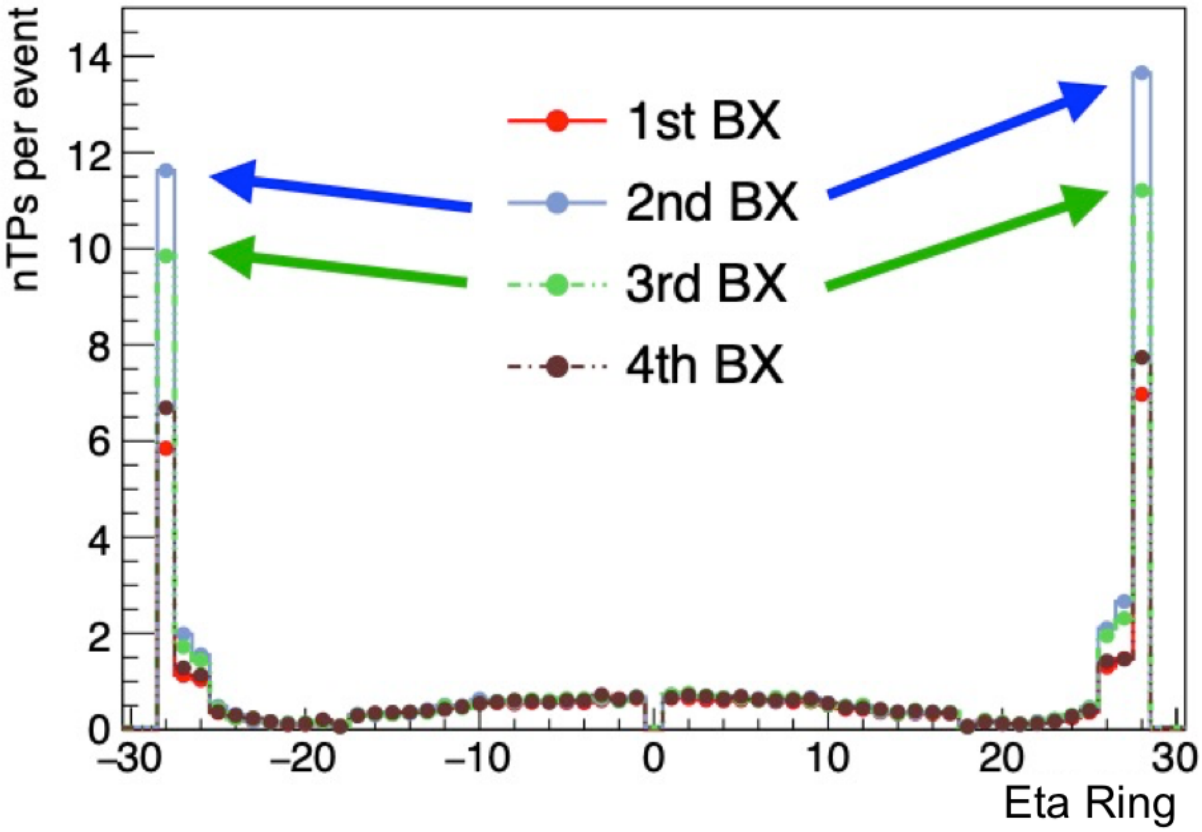

Figure 12: Number of ECAL TPs against the eta ring position for an 8b4e fill. TPs from the second bunch position in the 8b4e trains are shown in light blue. From Fill 6318. Figure from [25].

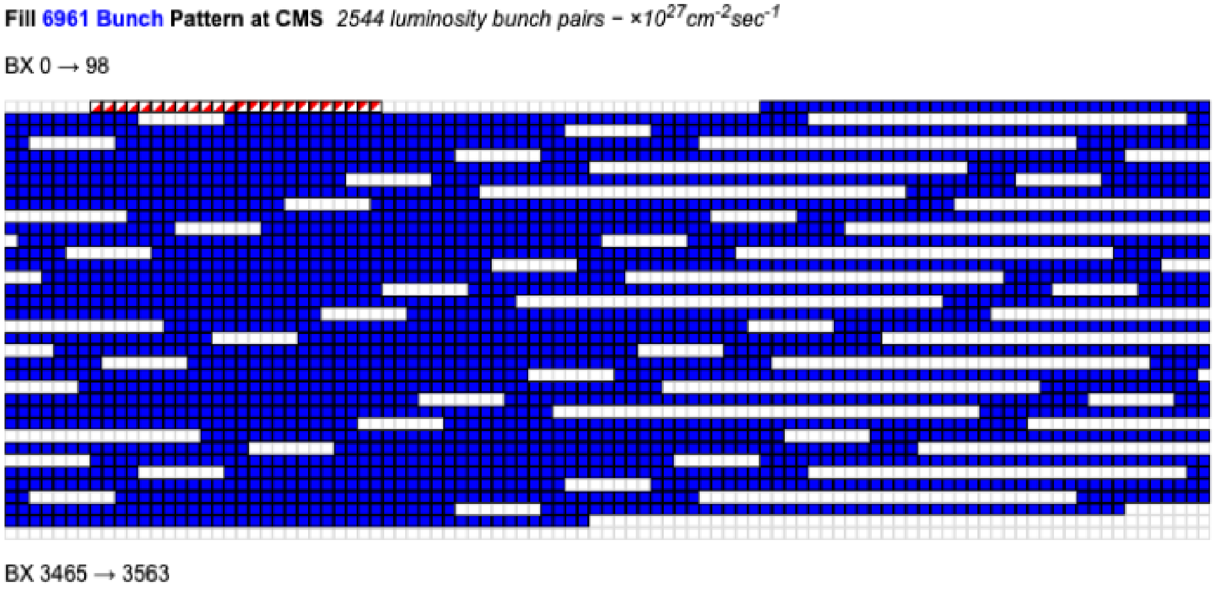

Figure 13: Example of a 48b bunch filling scheme from Fill 6961, recorded in July 2018. The blue boxes indicate a proton bunch. Figure from CMS Web Based Monitoring.

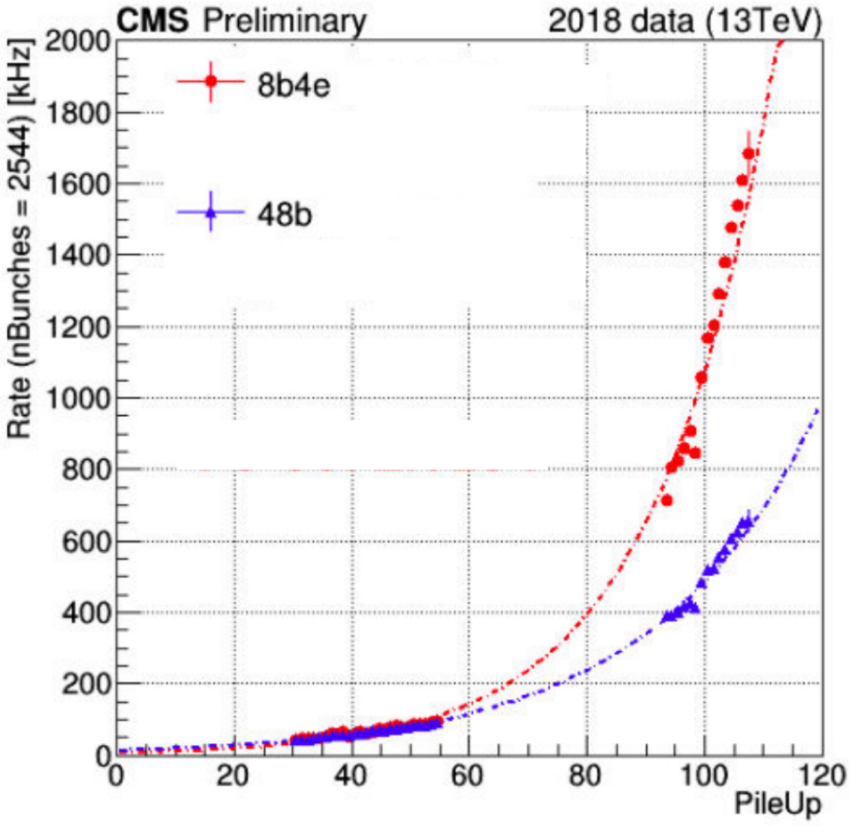

Figure 14: Measured rate against PU, for both the 8b4e and 48b bunch filling schemes. Data from a special high PU mixed filling scheme run in 2018. Figure from [26].

# 4 Current TP Performance

## 4.1 Amplitude Reconstruction Bias Study

An amplitude reconstruction bias study was conducted using data from June 2018 to evaluate the current performance of the weights used in forming the ECAL TPs. The data was used to derive parameterised average pulse shapes using the analytic function from section 2.2.3 for every ECAL crystal, in the absence of PU. A program was written to simulate the pulse shape for each crystal with a known true amplitude, calculate the signal value from the pulse shape at time intervals of 25 ns and multiply the signals by each of the weights (Equation 1 and Figure 5). This simulates the functions performed in the ECAL front-end boards. The five values are then summed and the bias from the amplitude reconstruction can be plotted. The bias is calculated as follows:

$$\text{bias} = \frac{A_{\text{rec}}}{A_{\text{true}}} - 1 \quad , \tag{4}$$

where $A_{\text{rec}}$ is the reconstructed amplitude and $A_{\text{true}}$ is the true amplitude. A bias of 0 corresponds to a set of weights that perfectly reconstruct the true amplitude of the pulse.

Using the current weights (Table 1), histograms are plotted showing the amplitude reconstruction bias in different eta regions, as shown in Figures 15-17. The average bias increases in higher eta regions, with a positive bias of 4% in eta ring 28. The spread is large, and consistently greater than 1% across all EE regions. The average bias across EE is 2.2% with a spread of 1.4%. The average bias in the barrel is 1.0% with a much smaller spread of 0.3%. This difference between EE and EB can be attributed to the higher levels of irradiation and damage in the EE crystals (Figure 7).

Across EE-/EE+ and EB, the current weights are overestimating the amplitude of the signal pulse by 2.2% and 1.0% respectively. This provides further evidence that the average pulse shapes of the crystals have changed significantly, causing a decrease in the amplitude reconstruction performance.

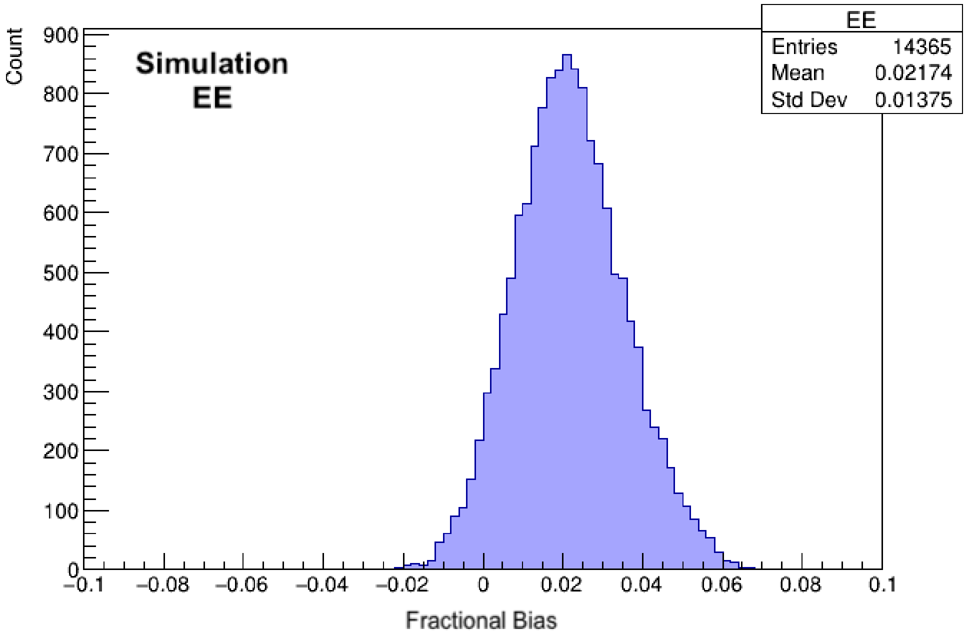

Figure 15: Amplitude reconstruction bias with the current weights in EE. Simulation study performed using pulse shapes derived from June 2018 data.

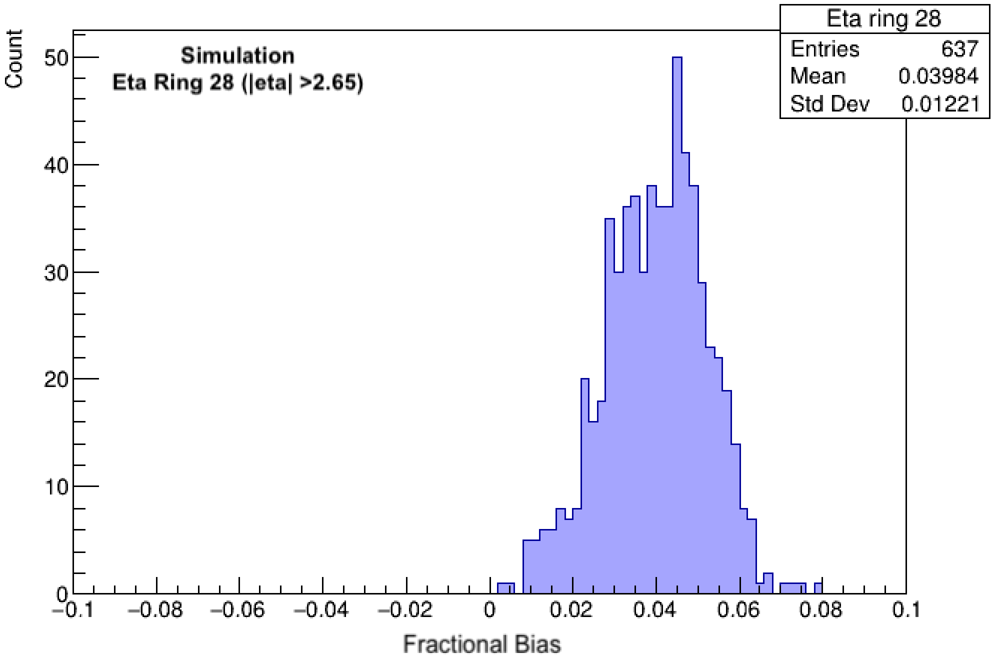

Figure 16: Amplitude reconstruction bias with the current weights in EE eta ring 28 ($|\eta| > 2.65$). Simulation study performed using pulse shapes derived from June 2018 data.

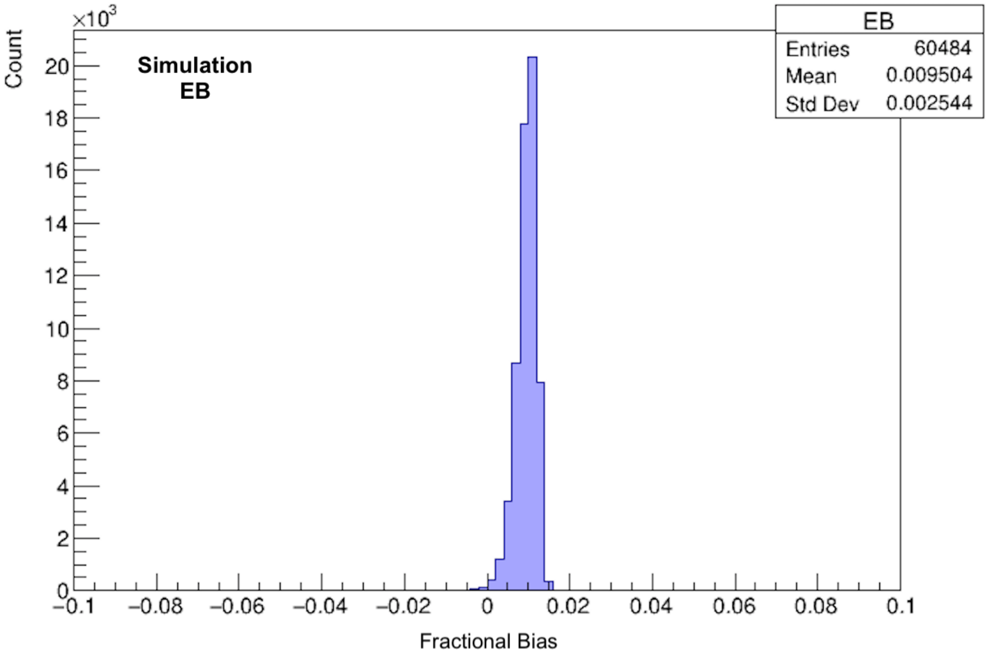

Figure 17: Amplitude reconstruction bias with the current weights in EB. Simulation study performed using pulse shapes derived from June 2018 data.

## 4.2 Online/Offline Energy Comparison using 2018 CMS Data

An alternative method for evaluating the performance of the weights can be obtained from CMS event data, by comparing the TP energies to the corresponding offline energies. This offline energy is calculated off-detector using complex and time-consuming algorithms that use PU templates to subtract out-of-time PU from the signal [27]. This provides the most accurate energy measurement possible in the presence of PU. By making this comparison in different regions of the detector, the performance of the TPs can be studied.

Code from the ECAL Prompt Feedback Group was adapted in various ways to make it suitable for retrieving the relevant online and offline energies, and was applied to CMS event data recorded in July 2018 with a mean PU of 30. Firstly, the offline reconstruction algorithm was updated to better account for PU. Secondly, code was written to calculate the offline energies in the endcaps, which did not previously exist. Finally, programs were written to analyse the online/offline energies and create a series of plots.

Figure 18 shows the difference between the online TP energy and the offline energy in EE+. On average across EE+, the TPs are overestimating the energy by 0.30 GeV. However, in rings 18-26 it is being underestimated. This is also true for EE-. Large overestimates are present in eta rings 27 and 28, with an average overestimate in ring 28 of 0.88 GeV. As seen in Figure 19, the spread in ring 28 is also large, at 1.27 GeV.

## 4.3 Conclusions

As predicted, the current weights are no longer optimal for present-day conditions. There is a strong positive bias of 2.2% in EE and 1.0% in EB when the weights are used to reconstruct the amplitude of June 2018 average pulse shapes without any PU. There is a large spread of 1.4% in the endcap but less so in the barrel, where the radiation damage is smaller. Significant biases are also seen in July 2018 CMS data, which includes PU. The greatest discrepancies in online/offline energy are found in the high eta regions, where the TPs are significantly overestimating the energy. In ring 28, the average overestimate is 0.88 GeV with a spread of 1.27 GeV. This can unnecessarily increase the trigger rate, reducing the efficiency for triggering on real physics signals.

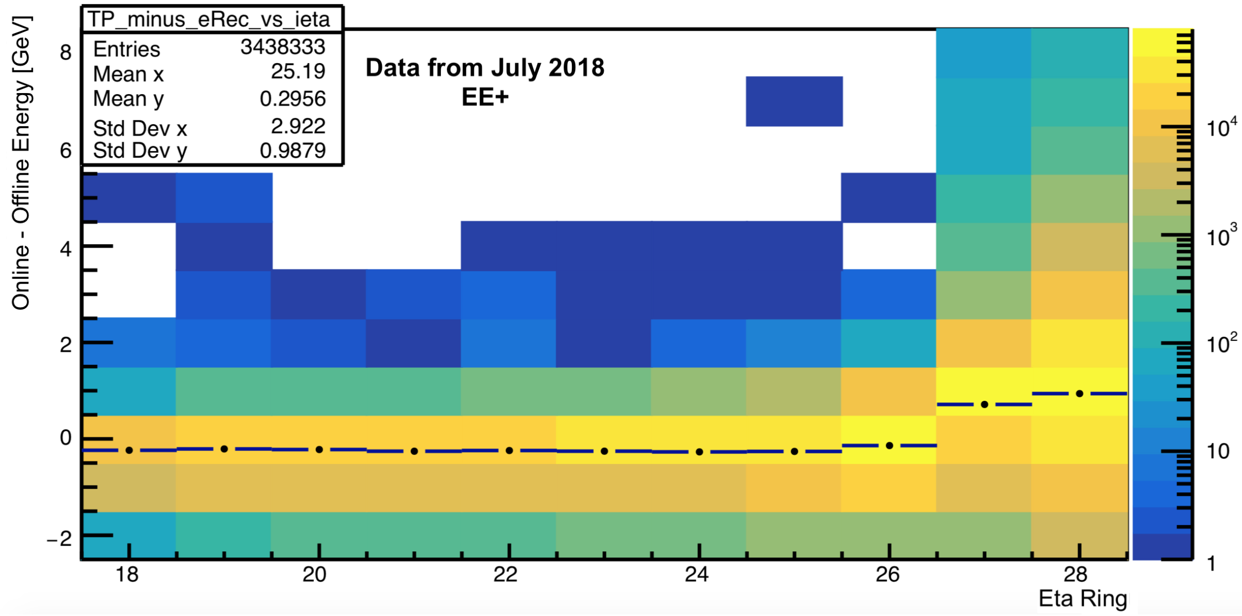

Figure 18: Online/offline energy differences with the current weights in EE+, from July 2018 CMS data. The colour of the z axis represents the number of counts in each bin. The black points with horizontal markers show the average value for each eta ring. The spreads are not plotted here due to their size, but can be seen for ring 28 in Figure 19.

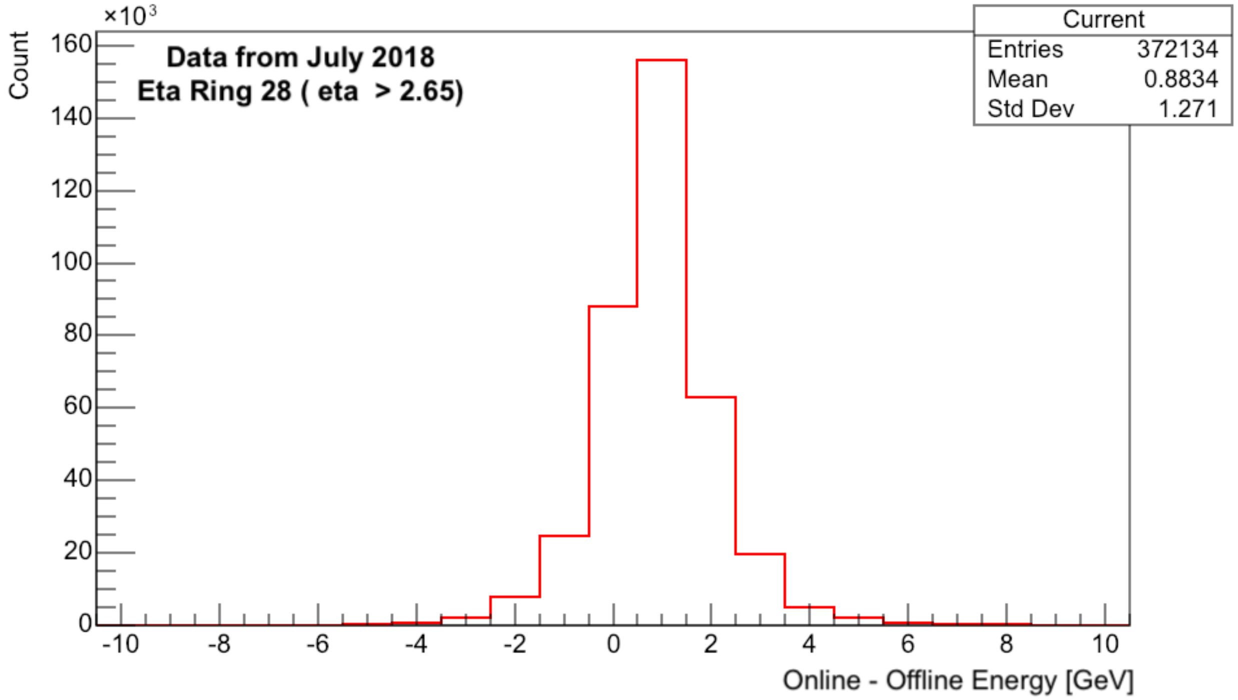

Figure 19: Online/offline energy differences with the current weights for ring 28 in EE+, from July 2018 CMS data.

# 5 Updated Weights

Updated weights were calculated [28] using the individual pulse shapes from data (see section 4.1) instead of the template pulse (see section 2.2.3). This provides a set of weights per crystal that are based on current detector conditions, calculated to reconstruct the signal amplitudes with zero bias.

Sets of average EE and EB weights were then computed by averaging the individual crystal weights across each EE/EB region, from now on referred to as ‘new avg’. When calculated, the weights are in decimal form. However, the weights must be encoded into the format the detector electronics can read. This process involves a rounding step and is outlined in section 6.1. The updated ‘new avg’ weights are as follows:

| | w1 | w2 | w3 | w4 | w5 |
|---|---|---|---|---|---|
| EE | -0.625000 | -0.515625 | 0.265625 | 0.500000 | 0.375000 |
| EB | -0.546875 | -0.546875 | 0.250000 | 0.484375 | 0.359375 |

Table 2: Updated ‘new avg’ EE and EB weights, optimised for June 2018 detector conditions.

## 5.1 Amplitude Reconstruction Bias Study

The updated ‘new avg’ weights (Table 2) were encoded and used for the same amplitude reconstruction study as section 4.1, and the results are shown in Figures 20-21.

In EE+, although a negative bias remains, the magnitude of the bias is halved. The spread is also reduced slightly. In EB, the average bias is reduced but the spread increases slightly. Using updated weights offers some improvement in the average amplitude reconstruction bias, but is limited by only being an average set of weights for EE/EB. Further improvements are expected when weights are applied on a per eta ring or per strip basis, as shown in section 6.

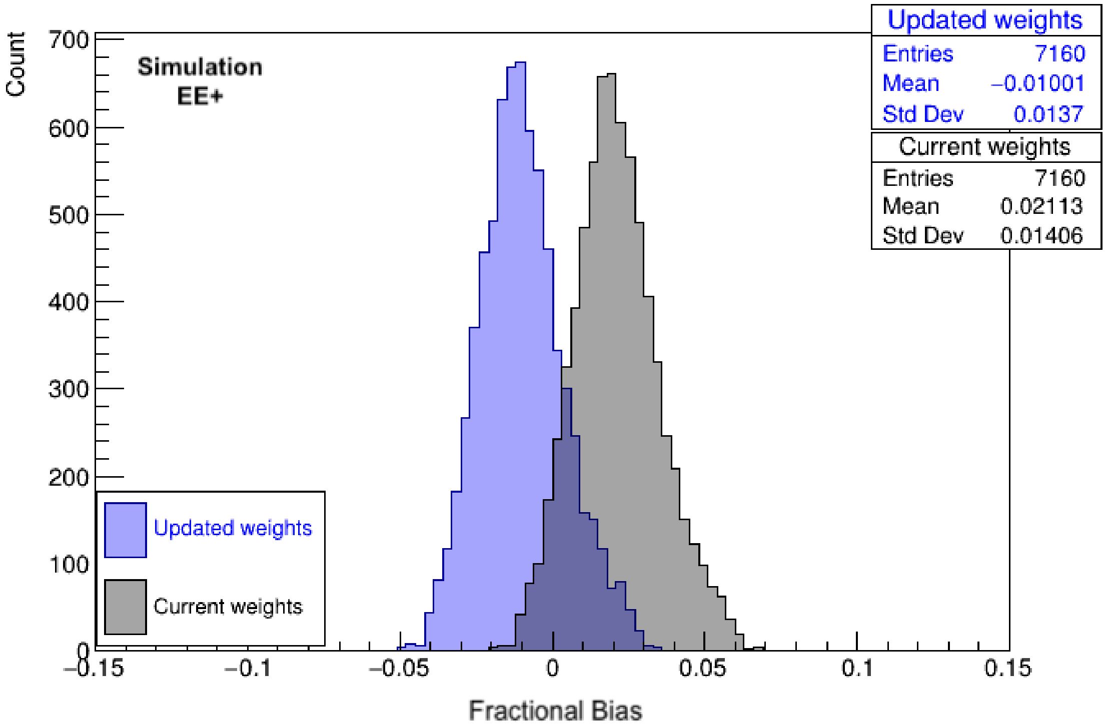

Figure 20: Amplitude reconstruction bias with the updated ‘new avg’ weights in EE+, shown in blue. Simulation study performed using pulse shapes derived from June 2018 data.

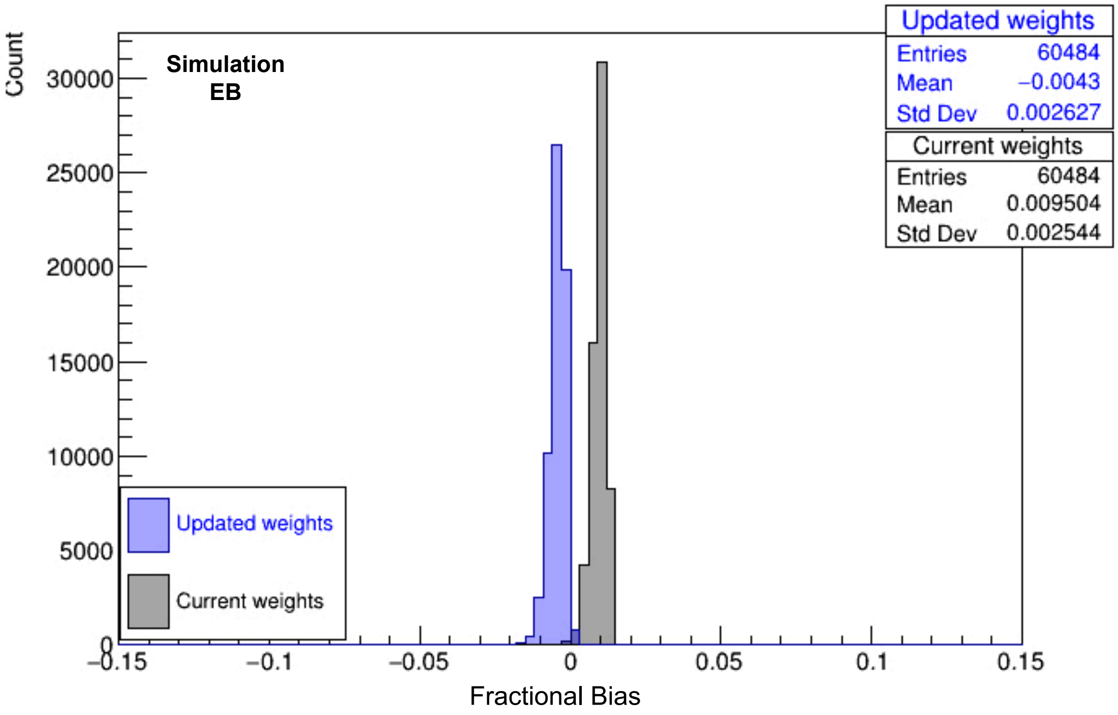

Figure 21: Amplitude reconstruction bias with the updated 'new avg' weights in EB, shown in blue. Simulation study performed using pulse shapes derived from June 2018 data.

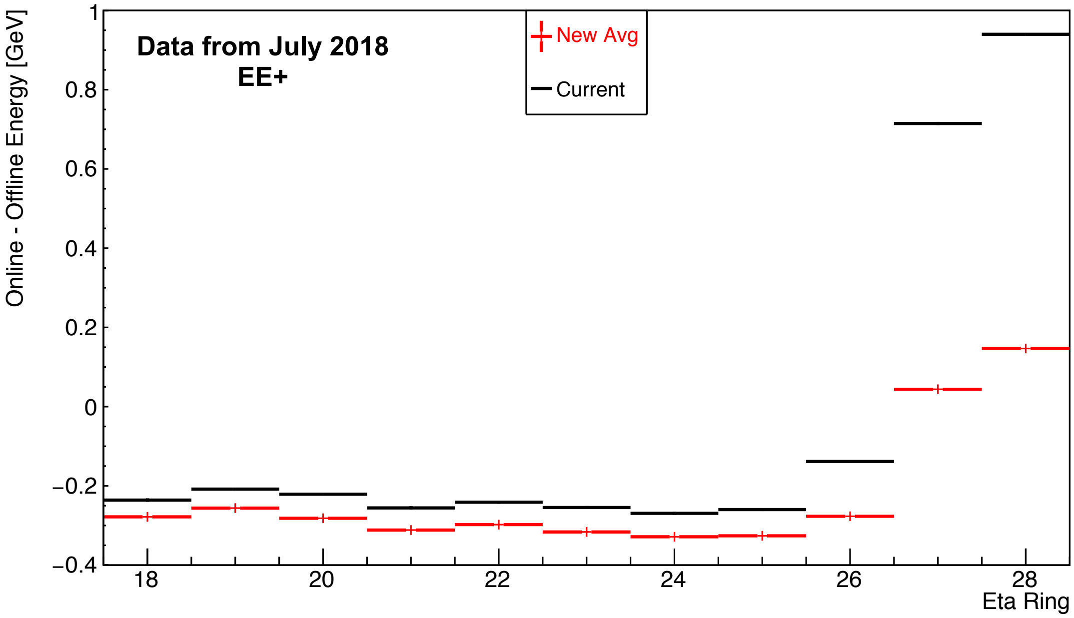

Figure 22: Comparison of online/offline energy differences with the updated 'new avg' and current average weights in EE+, using data from July 2018. The spreads are too large to plot here and the standard error on the means too small.

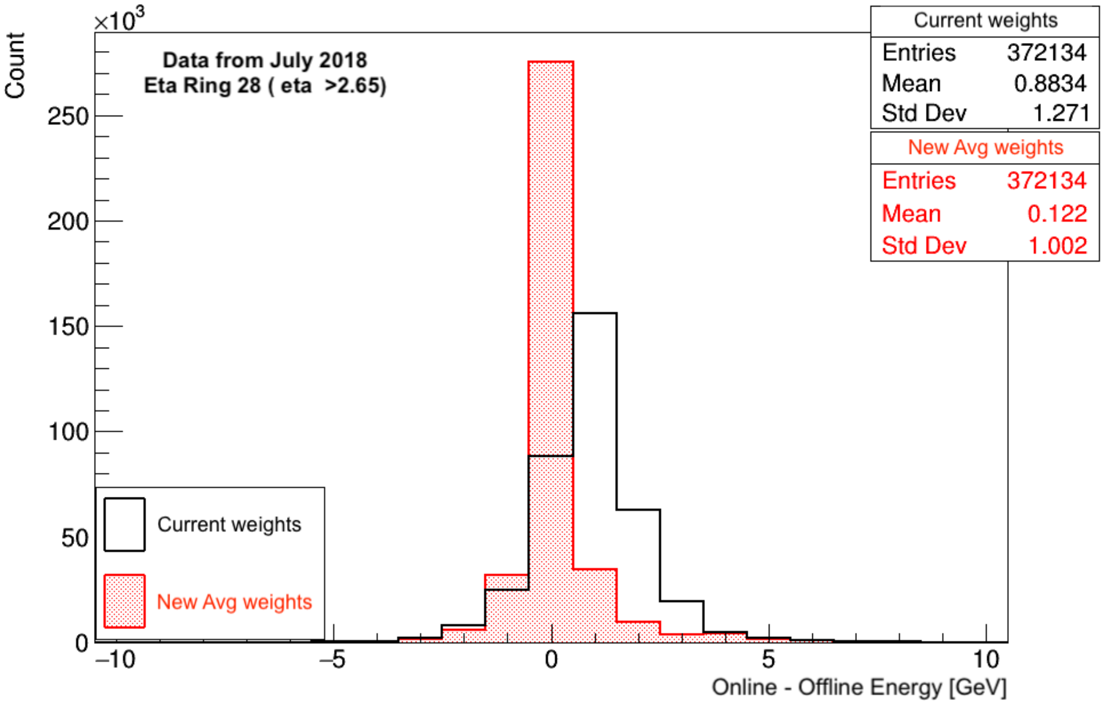

Figure 23: Comparison of online/offline energy differences with the updated 'new avg' and current average weights, plotted for EE+ eta ring 28, from July 2018 data.

### 5.2 Online/Offline Energy Comparison using 2018 CMS Data

The updated 'new avg' weights were loaded into the CMS database and used for the re-calculation of TPs within an emulator, which is designed to perform the TP generation algorithm from Figure 3 using CMS event data, but in software. Code was written to retrieve the emulated TP energies from the same dataset as section 4.2. This will provide a direct comparison between the current weights and new average weights of the same granularity.

The online/offline energy difference is reduced in the high eta rings 27 and 28 with the updated weights, as seen in Figure 22. However, in the lower eta rings there is an increase in the difference. From Figure 23, it is clear that by updating the weights, the positive bias and large spread are greatly reduced in ring 28. With a finer granularity of weights, it is possible that the bias and spread could be further reduced and the performance at lower eta rings improved.

### 5.3 Conclusions

It has been shown that by updating the weights, based on current conditions, the average positive bias and spread in the reconstructed amplitude are reduced, especially in the higher eta regions. However, a bias and spread remain. The online/offline energy bias is greatly reduced in high eta rings but is increased in lower eta rings, which could be improved by recalibrating the TPs. Increasing the granularity of the weights from being averaged across the EE/EB regions to per eta ring or per strip could further improve the performance. This will be investigated in the following section.

# 6 Increased Weight Granularity

Using the same pulse shape data as section 4.1, weights were calculated with the following granularities: per eta ring, per strip (best achievable on-detector) and per crystal (theoretical best). To calculate these, code was written to locate the crystals present in each of the eta rings and average the weights across the ring, to provide 56 sets of weights for the 56 eta rings in ECAL. More code was written to look up the five crystals present in each strip and average the five sets of weights across the strip, to provide 15176 sets of per strip weights. These weights were then encoded, and the process will now be described in detail, as it places a limit on the number of weights that can be applied in hardware.

## 6.1 Encoding Weights

Although having precise weights for each crystal would give the best amplitude reconstruction performance, this is not achievable in practice. Firstly, the finest granularity possible on-detector is per strip, as the weights are applied after summing the signals from five crystals in a strip (see Figure 4). Secondly, the encoding process involves rounding the weights to the nearest multiple of 1/64, and so only a finite number of discrete decimal weights are permissible. For example, calculating the decimal weights with a per strip granularity yields 1468 unique sets of decimal weights in EE+, but once encoded this reduces to 74, as shown in Figure 24.

This means that if the decimal weights do not vary by at least 1/64, they will be encoded into the same weights once applied in hardware. As the endcaps have been heavily irradiated and the crystal pulse shapes vary considerably between adjacent crystals, a large number of different encoded weights are still possible, as seen in Figure 24. However, in the barrel, where the radiation is much lower and pulse shapes have barely changed, the weights do not vary considerably enough to be encoded into different on-detector weights. Therefore, the following analysis and studies will focus on the ECAL endcaps, although the same procedure can be applied to EB in the future.

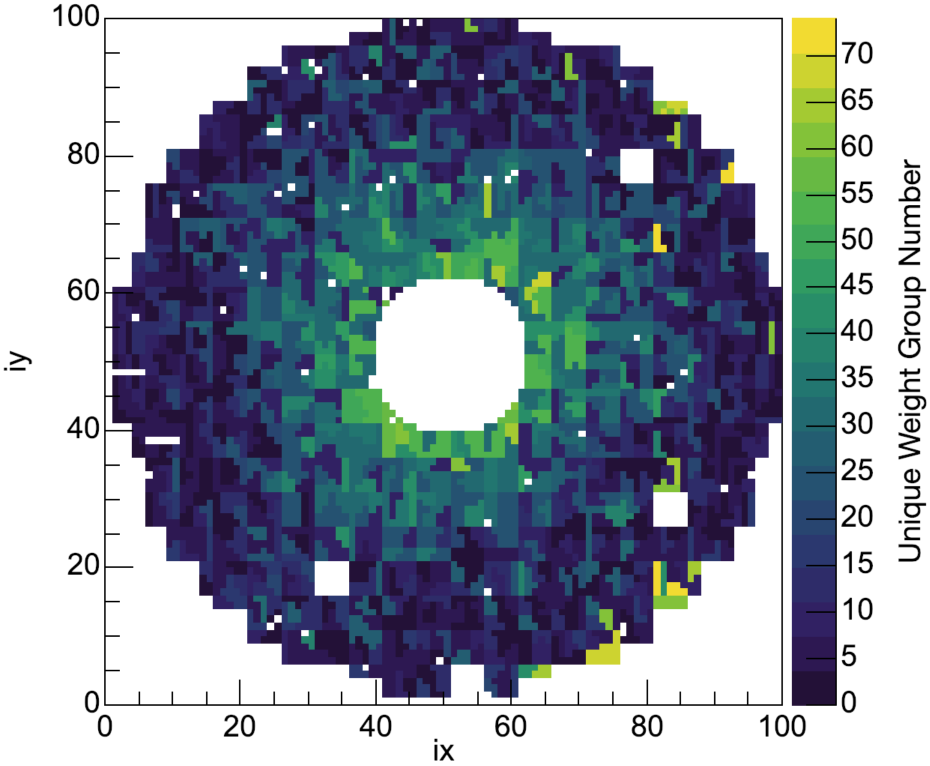

Figure 24: Number of unique sets of weights for 2018 conditions when weights are calculated with a per strip granularity in EE+ and encoded.

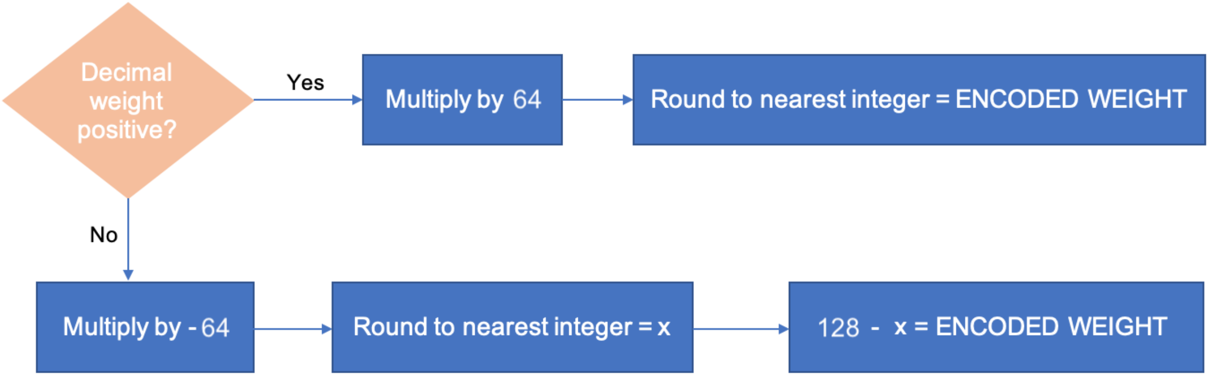

Figure 25: Weight encoding algorithm. Repeated for each weight.

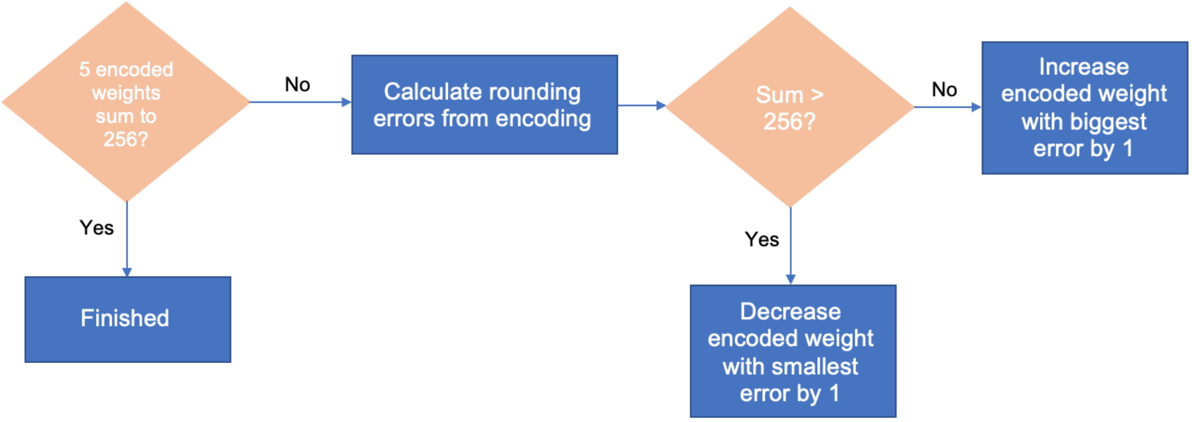

Figure 26: Encoded weights correction algorithm. This is repeated until the first condition is met.

The encoding process was reverse-engineered from current encoded weights, and is described in Figure 25. Once all five weights are encoded, a correction takes place, shown in Figure 26, which ensures that the weights still sum to zero (Equation 2).

### 6.2 Amplitude Reconstruction Bias Study with Increased Weight Granularity

The method described in section 4.1 was repeated with the different weight granularities listed in section 6, to compare the amplitude reconstruction performance on June 2018 pulse shapes with no PU. The results are plotted in Figure 27. Without the encoding process, the black per crystal histogram would be a vertical line at zero, i.e. with zero bias. However, the encoding introduces a small bias and spread in the amplitude reconstruction, which cannot be avoided or reduced. Updating the weights to 'new avg' slightly reduces the spread and halves the bias when compared to the current weights but a 1% negative bias remains. However, a much more significant improvement is seen when increasing the granularity to per ring and per strip. In fact, per strip weights offer performance not far from the theoretical best case of per crystal. This result is extremely encouraging and provides good motivation for applying the more granular weights to recent CMS data, in the presence of PU.

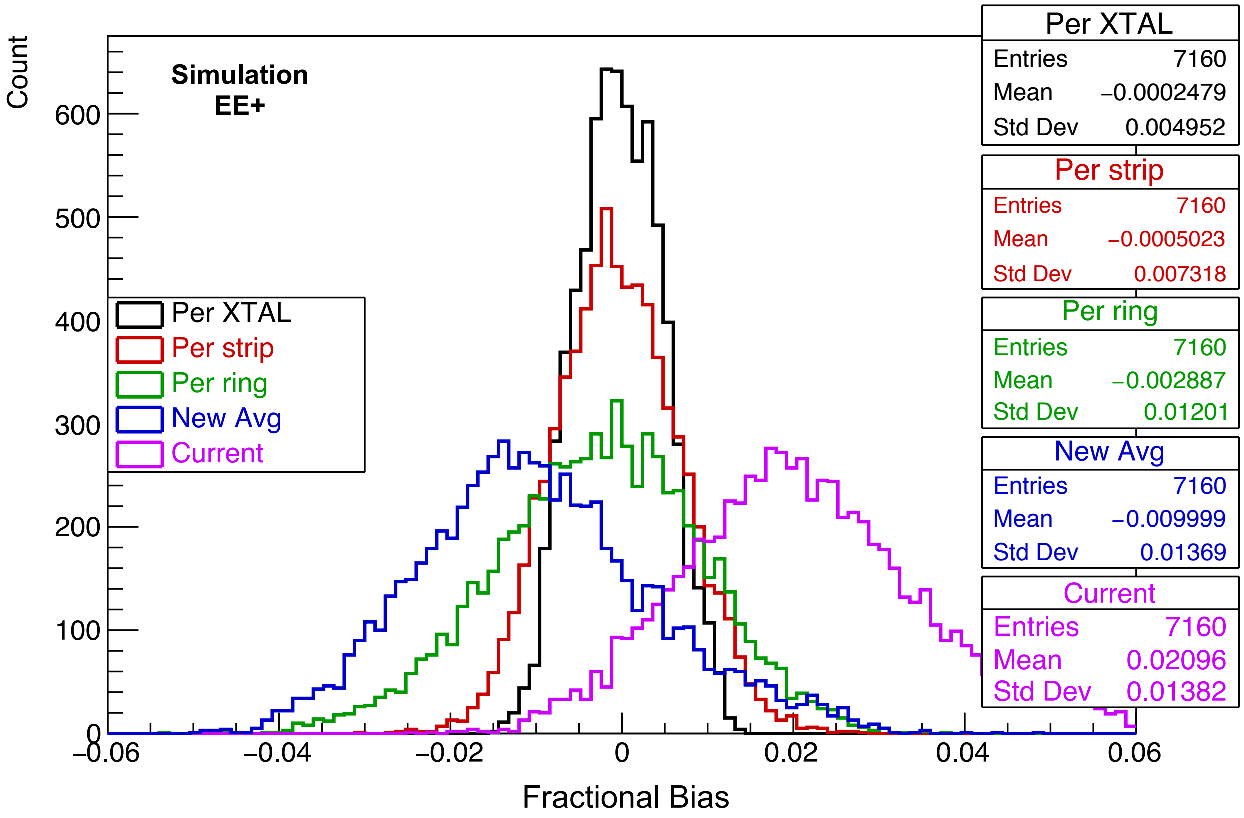

Figure 27: Amplitude reconstruction bias for different weight granularities in EE+. Simulation study performed using pulse shapes derived from June 2018 data.

### 6.3 Online/Offline Energy Comparison with Increased Weight Granularity

Weights with an increased granularity of per ring and per strip were loaded into the emulator and the TPs were recalculated and retrieved. Figure 28 shows the online/offline energy difference across the EE endcap rings. A large positive bias is present with the current weights in ring 27 and 28 and this is significantly reduced when updated weights are used. Any improvement of increasing the granularity from per ring to per strip is not visible, and is not as significant as predicted by the amplitude reconstruction bias study, performed in the absence of PU. This suggests that PU has a very large effect on the energy reconstruction. When looking only at ring 28 in Figure 29, the small differences between the increased granularity weights become more evident. As the granularity of the weights increases, the average energy difference and spread reduces. This trend is true at lower eta rings, but becomes smaller. This is unsurprising, as the lower eta regions have been damaged significantly less by the LHC beams.

### 6.4 Conclusions

Clearly, updated weights of any granularity perform significantly better than the current weights. The large improvements from an increased weight granularity suggested by the amplitude reconstruction bias study are not as clear when looking at the online/offline energy difference present in 2018 CMS data, which contains PU. Although small, there are still improvements in the bias and spread when using the per strip granularity when compared to the new average or per ring weights. It is clear that PU has a very significant contribution to the reconstructed energy, and the improvements seen with greater granularity are limited by it. This suggests that if per strip weights were computed to be optimised for the level of PU that matched the CMS data, further reductions in the bias and spread could be possible.

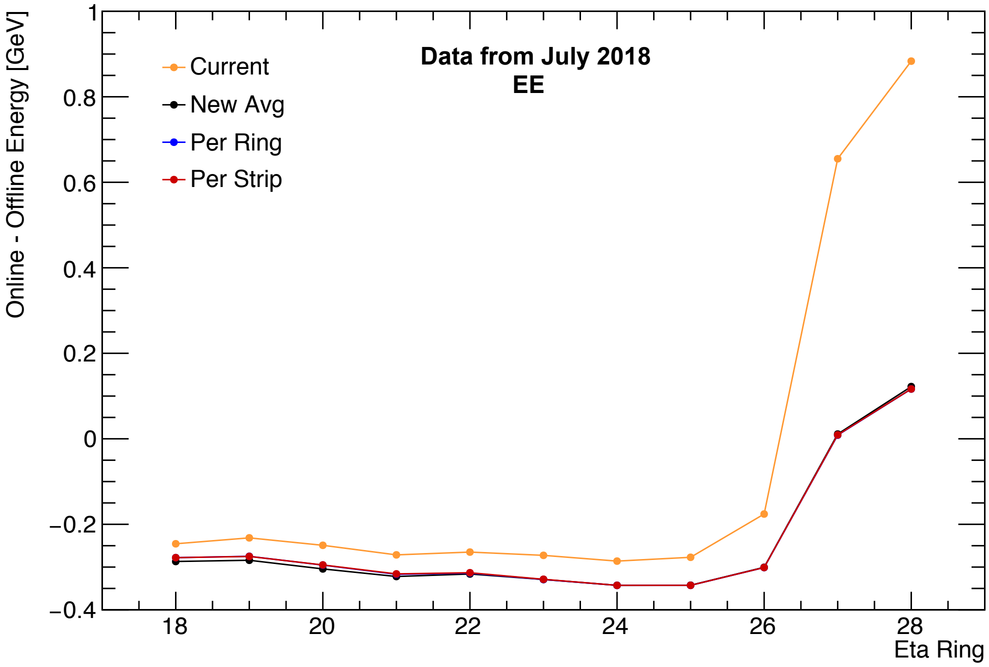

Figure 28: Online/offline energy difference across EE. The blue 'Per Ring' points are indistinguishable from the 'Per Strip' points. Data from 2018 run 320065. The spreads are too large to plot here and the standard error on the means too small.

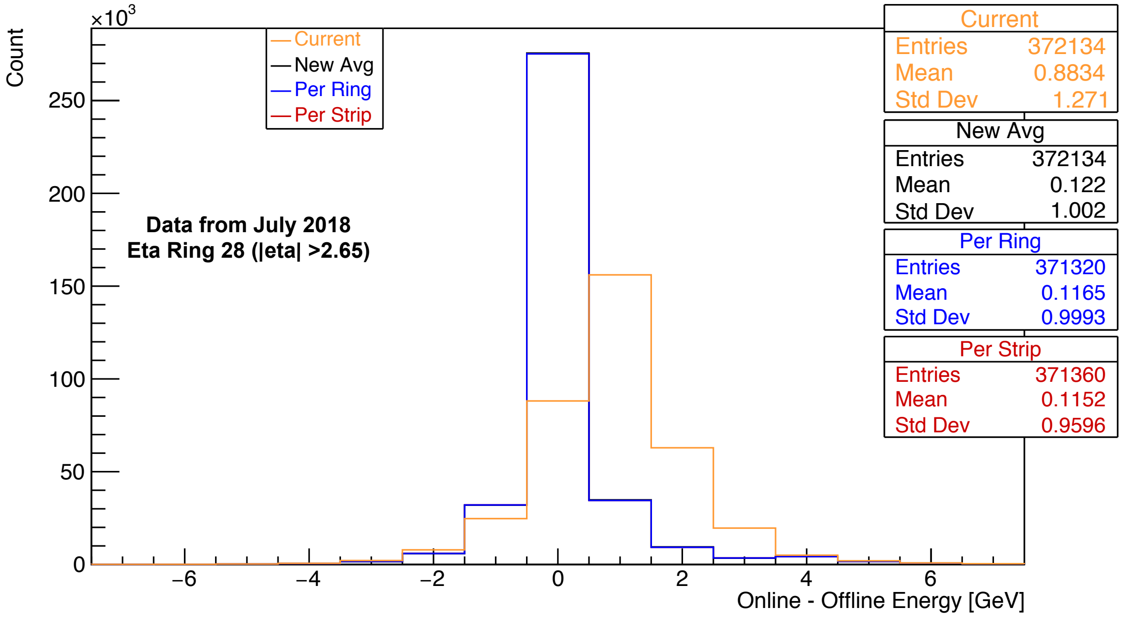

Figure 29: Online/offline energy difference in ring 28. Data from 2018 run 320065.

# 7 Pileup Optimised Weights

At the high luminosities used in LHC Run 2 (2015 - 2018), and the even higher luminosities planned for Run 3, signals from multiple bunch crossings overlap in the same crystal. These signals constructively interfere, such that the observed signal contains contributions from multiple pulses and bunch crossings, as seen in Figure 9. This PU effect is especially present in the inner rings of the ECAL endcaps. In the previous chapters, all updated weights used so far have been calculated from June 2018 average pulse shapes, which do not account for the effects of PU. Using non-PU-optimised weights on CMS data with large levels of PU will not provide the best possible amplitude reconstruction performance. Indeed, as seen in the previous section, the performance improvements from weights with an increased granularity seems to be limited by the PU contributions.

A Monte Carlo (MC) simulation was created [29], that replicates the LHC bunch train and PU present in the detector and the effect this has on the average pulse shapes in each crystal. From these PU-modified crystal pulse shapes, weights were computed that are optimised for a specific PU level and signal value. Figure 30 shows how the weights change when optimised for different levels of PU. This suggests that the per strip weights will be affected significantly enough by the PU that the weights will be encoded into a greater number of unique weight sets than were present without PU in section 6.1. Furthermore, the effect PU has on the weights can be seen. The first two weights, which are negative, become more negative in order to better subtract contributions from out-of-time pileup, while the three weights on the pulse become larger. The greater the PU, the more negative the first two weights become.

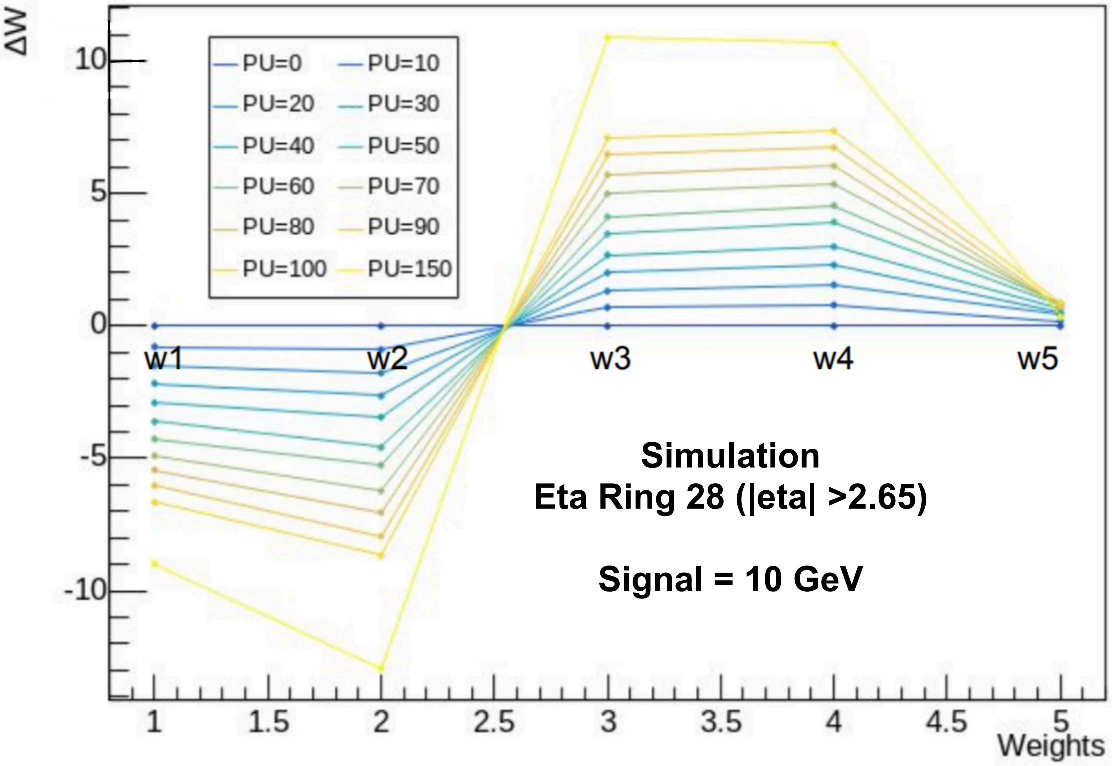

Figure 30: Result of the PU MC Simulation. The effect PU has on the five weights can be seen. The y axis is in units of the smallest unit resolvable during the encoding process. Figure from [30].

### 7.1 Data Used

To provide a comprehensive comparison of the effects of updated, more granular and PU-optimised weights at different PU levels and with different bunch filling schemes, runs at PU 30 and PU 50 were chosen, for specific 2017 8b4e and 2018 48b fills. A period of time within each of the specified runs was selected that matched the desired PU level. In Figures 31 and 32, the location of the four data files within two LHC Fills are highlighted, showing their corresponding PU level.

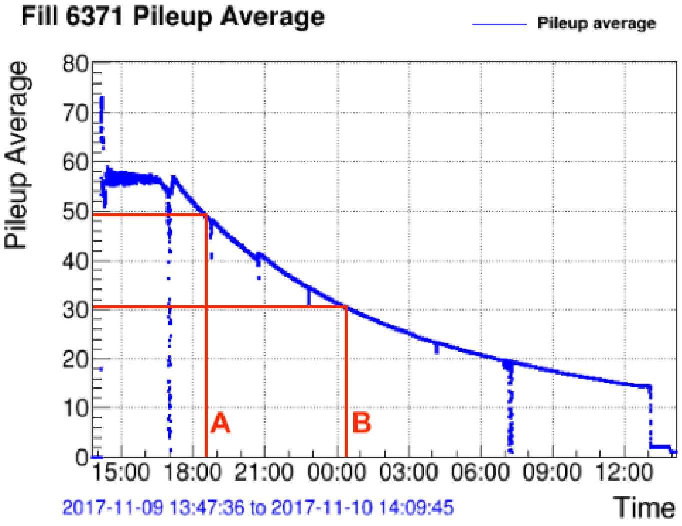

Figure 31: PU spectrum of Fill 6371, from November 2017. Letters A and B show the location of the PU 50 and PU 30 data respectively. From CMS WBM.

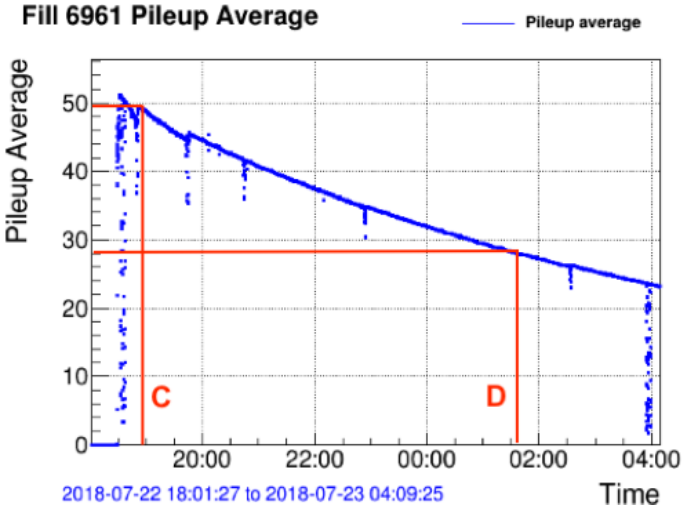

Figure 32: PU spectrum of Fill 6961, from July 2018. Letters C and D show the location of the PU 50 and PU 30 data respectively. From CMS WBM.

|  | 2017 8b4e | 2018 48b |
|---|---|---|
| PU 30 | B. 306459 | D. 320065 |
| PU 50 | A. 306456 | C. 320059 |

Table 3: Chosen runs corresponding to the two PU levels and two LHC bunch filling schemes.

## 7.2 Bias vs. Eta Ring

The online/offline energy bias was calculated for the eta rings across the endcaps for the current, new average, per strip and PU optimised weights. It was found that the PU optimised weights that performed best were when the PU level and signal energy (S) used for the weight computation matched the PU level and average energy of the TP spectrum from the CMS data. For clarity, only the best performing PU optimised weights are plotted below. Furthermore, to avoid repetition, only one PU level will be shown, as in all cases the trends are the same, just emphasised by a lower or higher PU. The bias in each eta ring was calculated as follows:

$$\text{bias} = \frac{\text{Online energy}}{\text{Offline energy}} - 1 \quad , \tag{5}$$

where the online and offline energies have been defined previously.

Three measures of performance are shown in Table 4, for both PU levels and both filling schemes. First, the bias averaged across the eta rings. Second, the 'flatness', defined as the spread of the biases from each eta ring, which gives an indication as to the uniformity of the response across the endcaps. Third, the average of the standard deviations of the bias from each eta ring.

### 7.2.1 8b4e Filling Scheme

For the following analysis, 2017 8b4e data is investigated. The different weights were calculated following the same process as for 2018 weights, except using pulse shapes measured from 2017 data. In Figure 33, the bias in each eta ring is plotted for PU 50 data. It is clear that the bias increases considerably in rings 26 to 28, where the average bias in the energy reconstruction with the current weights in ring 28 is 87%. The bias in the lower eta rings is made more negative with updated weights. The average bias across the rings is smallest for the PU 50 S2 weights, as seen in Table 4. Although the bias response isn't flat across the endcap, it is flattened for every updated weight configuration when compared to the current weights. PU 30 data follows the same trend, except with larger biases in the higher eta rings and smaller differences in each ring between the different updated weights. When looking at the bias across the endcaps at both PU levels, the improvements from a finer granularity and PU optimisation aren't immediately obvious. However, things become more clear when the spread in each ring is plotted. The spread in the bias represents the resolution of the TPs, and is plotted in Figure 34. Updating the weights to a new average reduces the spread in every eta ring. Furthermore, increasing the granularity to per strip and then PU optimised reduces the average spread further and this holds true for PU 30 too. In fact, with PU optimised weights on PU 50 data, the average spread is reduced by 29% from the current weights.

At a higher PU level, PU optimised weights perform significantly better than the other updated weights in terms of the average spread. This is unsurprising, as the per strip weights, which are not PU optimised, will not subtract as much of the large out-of-time PU contribution from the pulses. For every weight configuration, the average spread increases at PU 50 compared to PU 30, due to the increase in out-of-time PU contribution.

A reduction in the spread is an important measure of improvement when assessing different weights. Although reducing the average bias and flattening the response across the endcaps is beneficial, any eta-dependent bias can be removed with a simple eta-dependent calibration factor. The spread, or resolution, cannot be improved with a simple re-calibration. It is a characteristic of the energy reconstruction algorithm. Therefore, a significant decrease in the spread equates to a tangible resolution improvement, which will lead to better trigger performance.

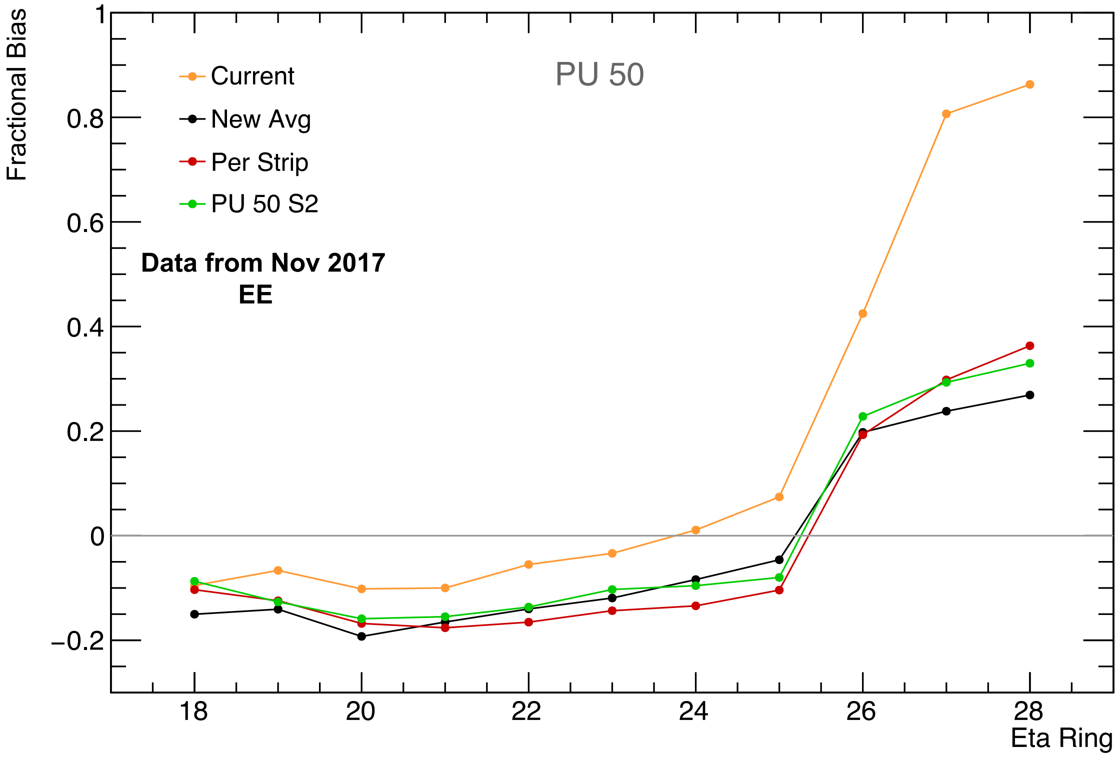

Figure 33: Bias against EE eta ring for 8b4e Run 306456 with PU 50. The spreads are too large to plot here and the standard error on the means too small.

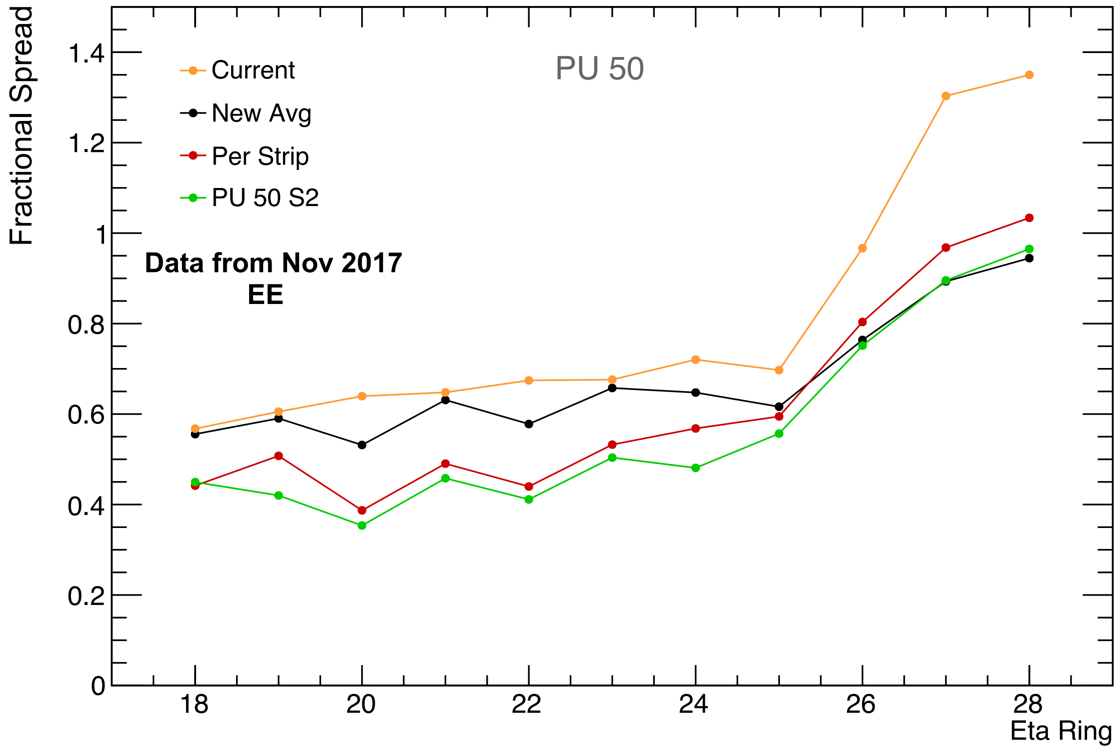

Figure 34: Spread against EE eta ring for 8b4e Run 306456 with PU 50.

### 7.2.2 48b Filling Scheme

Similar to the 8b4e case, PU optimised weights were calculated using 2018 data with the 48b filling scheme and the biases were computed and compared for the different weight configurations. The eta ring biases in Figure 35 for 48b are significantly smaller than in 8b4e. For example, the current weight bias in eta ring 28 for 48b is 57% that of 8b4e. This can be attributed to the larger out-of-time PU contribution within the 8b4e bunch filling scheme affecting the energy reconstruction accuracy. There is a much larger difference between the different weight configurations with 48b than with 8b4e. However, the overall shape is very similar. Furthermore, although the average spreads in 8b4e are much larger than in 48b, they increase less when changing from PU 30 to PU 50 than the 48b spreads.

From Table 4, it can be seen that PU optimised weights provide the flattest response across the endcaps and lowest average spread at PU 50. The current weights give the lowest average bias at both PU levels, but when combined with Figure 37 it is clear this comes as a result of the huge positive biases in rings 27 and 28 cancelling out the smaller negative biases across the other rings. At PU 30, the lowest spread is from the PU optimised weights and the flattest response from the per strip weights.

As seen before, PU increases the average spread across the endcaps and PU optimised weights reduce the spread more at high PU than at low PU. Figure 36 shows that the spread increases with eta ring. Interestingly, the average spread of the per strip weights is higher than with new average weights. Clearly, at high levels of PU, an increased granularity does not guarantee better performance.

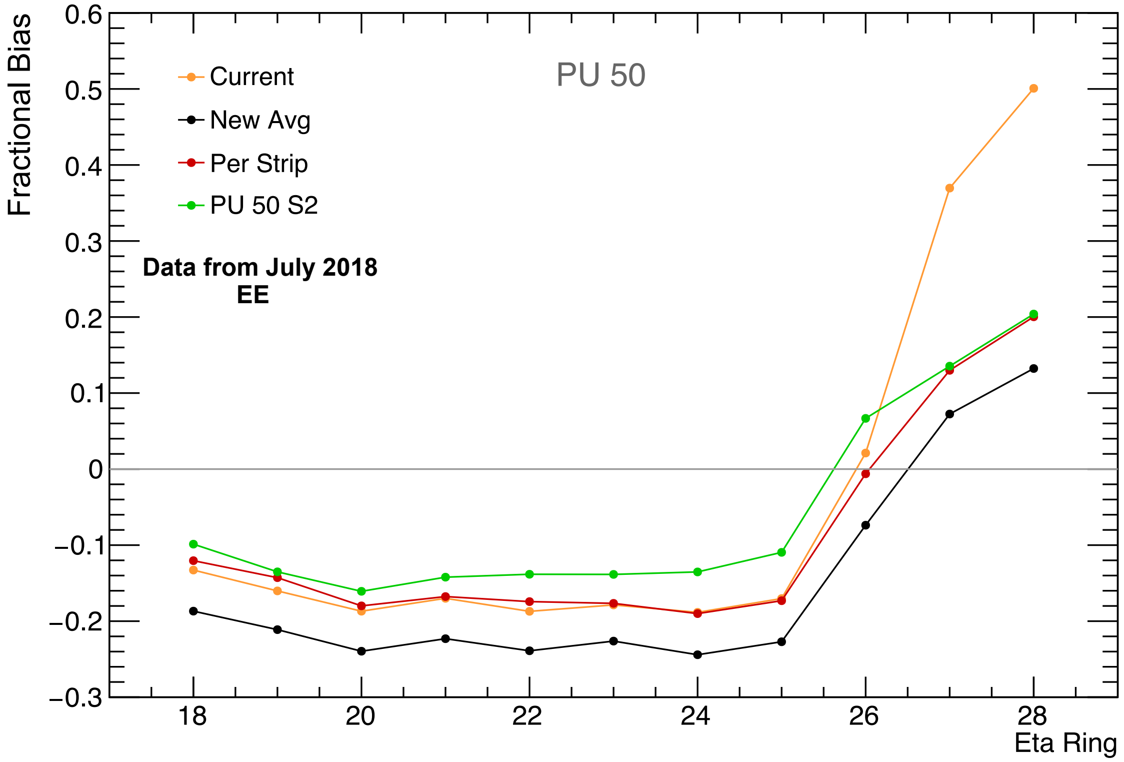

Figure 35: Bias against EE eta ring for 48b Run 320059 with PU 50. The spreads are too large to plot here and the standard error on the means too small.

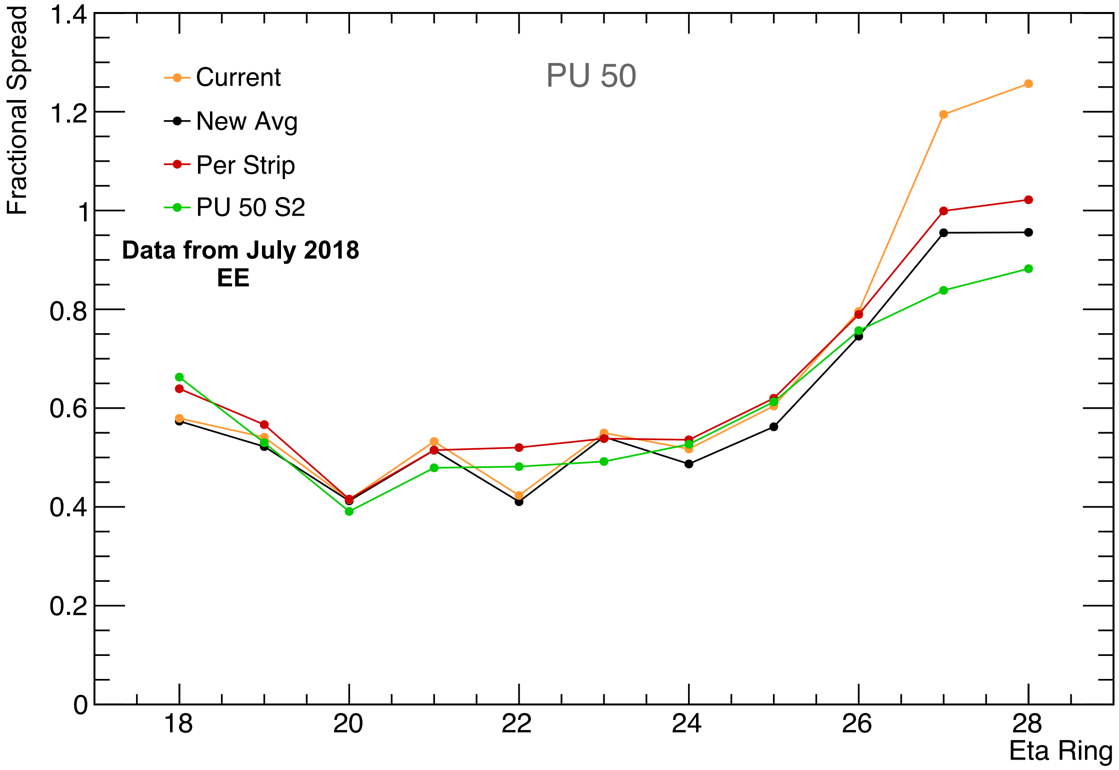

Figure 36: Spread against EE eta ring for 48b Run 320059 with PU 50.

### 7.2.3 Conclusions

For both bunch filling schemes and both PU levels, PU optimised weights matching the PU present in the data improve the resolution across the different endcap eta rings the most. In almost every case, an increased granularity to per strip reduces the spread compared to an average taken over the entire EE, and in all cases updated weights perform better than the current weights. PU optimised weights reduced the spread more significantly when at a higher PU level. As the luminosity and PU increase at the LHC, the use of PU optimised weights will become more necessary to maintain good energy reconstruction performance.

It is clear the choice of bunch filling scheme has an impact on the energy reconstruction bias across the eta rings of the endcaps. For the same PU level, the current weight bias in eta ring 28 with 48b is approximately half that of 8b4e. The average spread is also larger for 8b4e across the eta rings. However, there is a common trend. For both 48b and 8b4e, the average bias decreases and the differences between the weight configurations increases with an increasing PU level. Overall, it is clear that PU optimised weights reduce the eta ring dependence of the energy reconstruction bias and reduce the average spread more effectively than the other weight configurations.

| Data | Weights | Average Bias | Flatness | Average Spread |
|---|---|---|---|---|
| 8b4e PU 30 | Current | 0.1884 | 0.4411 | 0.8021 |
| | New Avg | -0.0092 | **0.2372** | 0.6681 |
| | Per Strip | -0.0154 | 0.2460 | 0.5857 |
| | PU 30 S2 | **0.0003** | 0.2465 | **0.5650** |
| 8b4e PU 50 | Current | 0.1570 | 0.3501 | 0.8044 |
| | New Avg | -0.0303 | **0.1672** | 0.6736 |
| | Per Strip | -0.0240 | 0.1939 | 0.6152 |
| | PU 50 S2 | **-0.0083** | 0.1818 | **0.5678** |
| 48b PU 30 | Current | **-0.0670** | 0.2420 | 0.5714 |
| | New Avg | -0.1356 | 0.1418 | 0.5203 |
| | Per Strip | -0.1334 | **0.1346** | 0.5182 |
| | PU 30 S2 | -0.1006 | 0.1464 | **0.5083** |
| 48b PU 50 | Current | **-0.0439** | 0.2346 | 0.6735 |
| | New Avg | -0.1515 | 0.1286 | 0.6073 |
| | Per Strip | -0.0910 | 0.1311 | 0.6510 |
| | PU 50 S2 | -0.0593 | **0.1237** | **0.6048** |

Table 4: Results for bias against eta ring for the different datasets and weight configurations. The different metrics are defined in the text. Numbers in bold are the lowest in the column and show the weight configuration that performs best for that metric.

## 7.3 Bias vs. Bunch Position

Every event in CMS has a bunch position (BX position) associated with it, which records the position in the bunch train where the event occurred. Code was written to look-up the bunch train configuration (Figures 11 and 13), and determine which position within the 8 proton or 48 proton repeating train the event originated from. A study was performed to investigate the dependence of the ECAL TP energy bias on position within the two bunch filling schemes. This was used to investigate where large biases exist and whether updated or more granular weights can reduce it. Three measures of performance, as defined in section 7.2, are shown in Table 5, for both PU levels and both filling schemes.

### 7.3.1 8b4e Filling Scheme

It has previously been shown in Figure 12 that the majority of TPs originate from the second and third position of the 8 position bunch train. This is believed to be due to the large energy bias in the same positions, and also explains why the L1 Trigger rates increase significantly when the 8b4e filling scheme is used.

Figure 37 shows the dependence of the bias on position within the 8 different bunches of the 8b4e filling scheme. With the current weights, there are large biases throughout 7 of the 8 positions. The largest biases are at positions 2 and 3, with a maximum bias of 80%, which explains why most of the TPs originate in these early bunch positions, as seen in Figure 12. There is a large variation in the bias across the positions, with a significant change between the last two, due to the rapidly changing PU profile. Updating the weights to any of the three new configurations significantly reduces the bias, halving it in some positions. Updated weights also flatten the bias response, but cannot completely remove the bunch position dependence. Although the 'new avg' weights give the lowest average bias as seen in Table 5, the flattest response and lowest average spread is from the PU optimised weights.

At lower PU, the average biases and spreads are actually larger and the variation of the bias between the different positions becomes more pronounced. Like PU 50, at lower PU the 'new avg' weights give the lowest average bias, and the PU optimised weights give the lowest average spread and flattest response. PU optimised weights are more effective at reducing the average spread from the current weights at higher PU, with a 29% reduction at PU 50 compared to a 27% reduction at PU 30.

### 7.3.2 48b Filling Scheme

A similar analysis was performed for the 48b filling scheme. Figure 38 shows a large variation in the bias across the first 10 and last 2 positions of the 48b bunch filling scheme, with a region of moderate stability in the middle of the bunch train. This variation is very large with the current weights, and a maximum bias of 70% is present at bunch position 2. Updating the weights to a new average set reduces the size of the variations at the beginning and end of the bunch train and also provides a more stable central region, however, a significant variation remains and a negative average bias is introduced. Increasing the granularity to per strip reduces the variation yet further and reduces the size of the introduced negative bias. With PU optimised weights, the best performance of the four weight configurations is achieved. The dependence of the bias on the bunch position is minimised and the average bias and spread across all positions is reduced the most too, as seen in Table 5.

Lower PU has a number of effects on the overall bunch position dependence of 48b. The large biases and large variations in the bias present at the beginning and end of the bunch train are 20% smaller and the variation across the positions is lower. Furthermore, the difference in performance between the 'new avg' and per strip weight configurations is much reduced. In this case at lower PU, an increased granularity does not yield significantly better results, but PU optimised weights still perform the best.

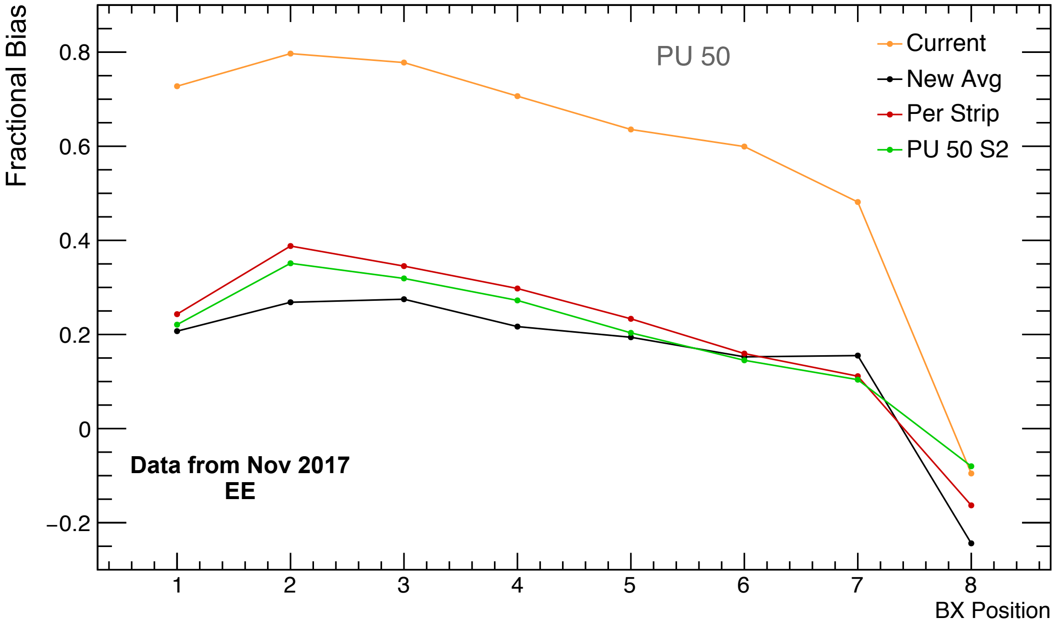

Figure 37: Bias against BX position for 8b4e Run 306456 with PU 50. The spreads are too large to plot here and the standard error on the means too small.

### 7.3.3 Conclusions

Across both bunch filling schemes and at high PU, large biases are present when using the current weights. There is a large variation in the bias for all bunch positions within the 8b4e scheme and for the first and last positions of the 48b scheme. However, 48b has a central region of stability, as the PU level (in-time and out-of-time) is constant here. Updated weights offer an improvement to the current weights for both schemes, and PU optimised weights provide the flattest response and reduce the spread across the bunch positions the most in all cases. Lower PU has the opposite effect on the biases present in the two filling schemes, where in 8b4e the bias is increased but in 48b the bias is reduced. However in both filling schemes, PU optimised weights provided better performance at higher PU than at lower.

It is clear to see why the 8b4e filling scheme was problematic for the L1 Trigger. The constantly changing out-of-time PU level causes a large energy bias and large variation in the energy bias across the 8 bunch positions, with the largest bias occurring in position 2, causing the majority of TPs to originate from this position. With no central region of stability, as seen with 48b, 8b4e is a challenge for any weights configuration. However, it has been shown that updating the weights, increasing the granularity and optimising for PU reduces the bias, reduces the bunch position dependence of the bias and reduces the spread, with PU optimised weights performing the best. This is true for both bunch filling schemes and both PU levels.

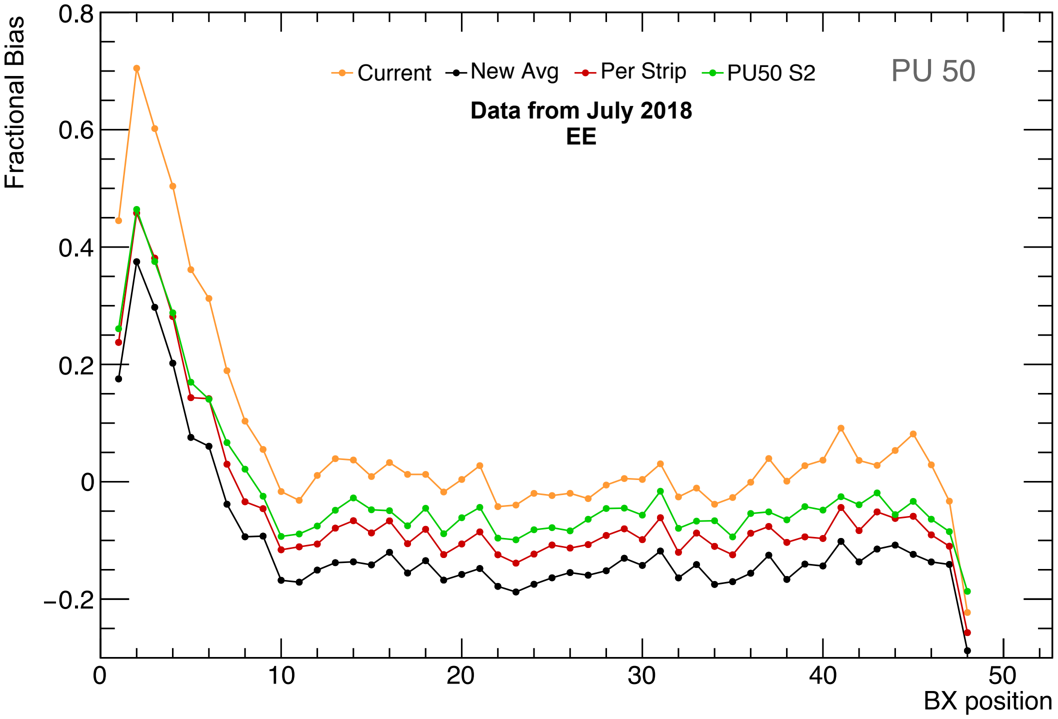

Figure 38: Bias against BX position for 48b Run 320059 with PU 50. The spreads are too large to plot here and the standard error on the means too small.

| Data | Weights | Average Bias | Flatness | Average Spread |
|---|---|---|---|---|
| 8b4e PU 30 | Current | 0.7899 | 0.2722 | 1.3924 |
| | New Avg | **0.2845** | 0.1564 | 1.0096 |
| | Per Strip | 0.3131 | 0.1452 | 1.0518 |
| | PU 30 S2 | 0.3224 | **0.1368** | **1.0151** |
| 8b4e PU 50 | Current | 0.5788 | 0.2723 | 1.2121 |
| | New Avg | **0.1531** | 0.1559 | 0.8828 |
| | Per Strip | 0.2012 | 0.1621 | 0.9266 |
| | PU 50 S2 | 0.1920 | **0.1289** | **0.8595** |
| 48b PU 30 | Current | 0.06812 | 0.1250 | 0.9029 |
| | New Avg | -0.0582 | 0.0911 | 0.7395 |
| | Per Strip | -0.0631 | 0.0889 | 0.7307 |
| | PU 30 S2 | **-0.0176** | **0.0888** | **0.7080** |
| 48b PU 50 | Current | 0.0692 | 0.1738 | 0.9097 |
| | New Avg | -0.1025 | 0.1247 | 0.7320 |
| | Per Strip | -0.0468 | 0.1333 | 0.7743 |
| | PU 50 S2 | **-0.0151** | **0.1244** | **0.6870** |

Table 5: Results for bias against BX position for the different datasets and weight configurations. Numbers in bold are the lowest in the column and show the weight configuration that performs best for that metric.

## 7.4 Bias vs. Energy

An investigation into the energy scales most affected by the updated weight configurations was conducted. It is important to have a clear understanding of which TP energies are changed by the new weights and at which energies the reconstruction performance is improved. Furthermore, any adverse affects of updating the weights or increasing the granularity must be studied. For example, if more granular weights improved the energy reconstruction at lower energy but introduced a large bias or spread at higher energy, they would be unsuitable for use in the high-resolution ECAL. The energy scale also determines the type of physics events that can be reconstructed more accurately. Low energies, around 2 GeV, are important for the missing energy triggers and are relevant for supersymmetry searches. Whereas, 30 GeV and upwards is a common energy for single electrons and photons, which must also be reconstructed accurately. Code was written to divide the TPs into energy bins so the bias and spreads could be studied as a function of energy. Only PU 50 was studied here, as this level is most relevant for the upcoming LHC Run 3 and should provide more representative results. For comparison, PU optimised weights optimised for signals of 2 GeV and 30 GeV are plotted. Three measures of performance are shown in Table 6, for both filling schemes at PU 50. These have been calculated for whole EE, rings 18 to 21, 22 to 25 and 26 to 28, to see the effects in the different eta regions.

### 7.4.1 8b4e Filling Scheme

Figure 39 shows the bias against energy for the whole EE. At energies of 3 GeV and below, there is a large bias present with the current weights and a large reduction in the bias when the weights are updated. Clearly, the energy reconstruction of low energy TPs is improved significantly, with smaller differences at energies greater than 8 GeV. A large difference can be seen when increasing the weight granularity from ‘new avg’ to per strip. PU 50 S30 weights perform similarly to per strip, except at higher energy where they reduce the bias more successfully. As seen in Table 6, the ‘new avg’ weights have the lowest average energy bias and average spread, but the PU 50 S2 weights have the flattest bias curve across the different energy bins.

Looking at rings 26 - 28 in Table 6, it is clear the behaviour occurring in these innermost rings dominates the whole EE. The majority of events occur in the innermost rings, and these events have large energy biases, thereby increasing the whole endcap average. As the eta ring increases, the flatness of the bias curve reduces and the average spreads increase. The best performing weight configuration changes, but is often the PU 50 S2 weights.

Looking at the spread in rings 26 to 28 at different energy levels, as seen in Figure 40, it is clear the improvements from more granular weights are once again seen mostly at low energy. The ‘new avg’ weight configuration actually has the lowest average spread across the energy ranges, followed closely by the PU 50 S2 optimised weights. Although, the ‘new avg’ weights do have a larger average bias. Between 3 and 8 GeV, the current weights have a marginally lower spread, but this is outweighed by the worse performance in the other energy ranges.

### 7.4.2 48b Filling Scheme

Similar to 8b4e, the greatest improvement from the current weights is seen at low energy. As seen in Figure 41, the green line of PU 50 S2 optimised weights brings the bias much closer to 0 across a large range of energies, from 3 GeV upwards. A large difference can be seen between these PU optimised weights and the other weight configurations. Furthermore, by 3 GeV, the bias is stable and the large positive biases at lower energy are only present in the first two energy bins. Looking at Table 6, it is obvious once again that the average behaviour across all rings of the two endcaps is dominated by the behaviour occurring in the innermost eta rings.

In every eta region, the flatness of the bias curve and the average spread are minimised when the PU 50 S2 weights are used. Figure 42 shows the spreads in the bias in the different energy ranges in eta rings 26 to 28. Interestingly, the average spread here is significantly less than in the 8b4e filling scheme and above 3 GeV the five weight configurations perform very similarly.

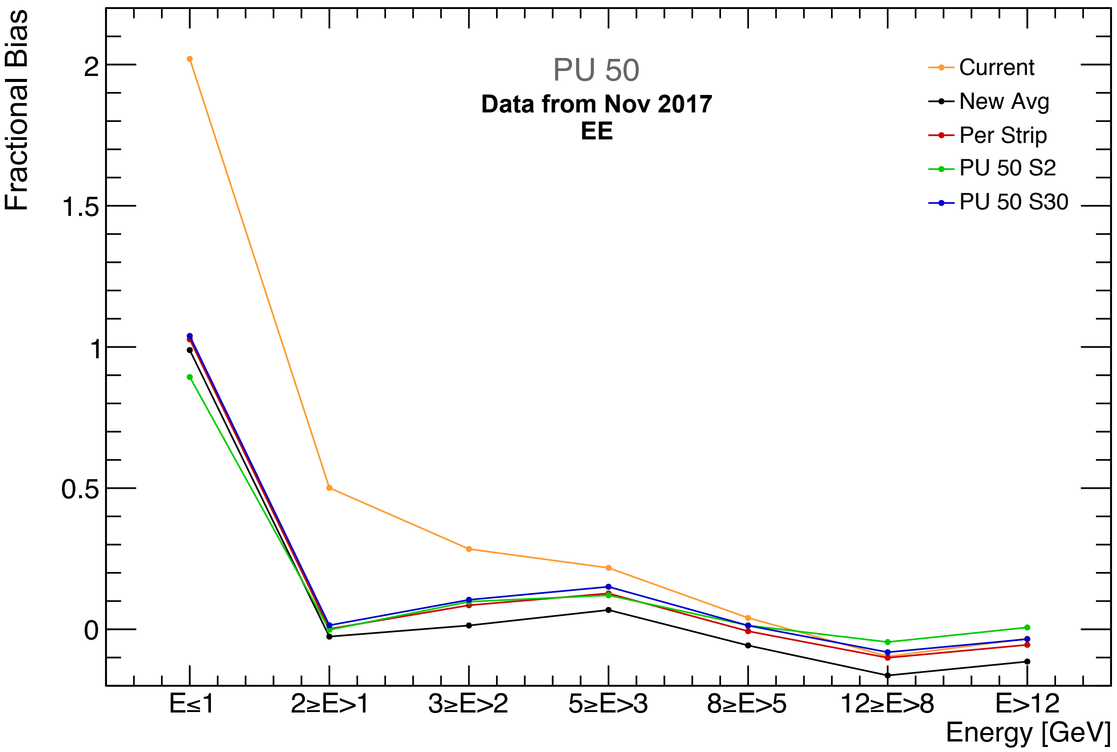

Figure 39: Bias against energy for 8b4e Run 306456 with PU 50 for all EE eta rings. The spreads are too large to plot here and the standard error on the means too small.

### 7.4.3 Conclusions

The biases present in the 8b4e filling scheme are larger at every energy range than for the 48b filling scheme. For both schemes, a large positive bias is present at low energy with the current weights, which is reduced significantly by updating the weights to any of the four updated weight configurations. However, in 8b4e, the large bias persists to a higher energy than in 48b, due to the larger differences in out-of-time PU contributions. Furthermore, the average spreads are larger in 8b4e and remain greater than 20% for all energy ranges. The average EE behaviour is dominated by the biases coming from the innermost eta rings in both filling schemes and significant improvements can be realised in these rings by updating the weights.

For 8b4e, the best performing weights configuration is not obvious. Although the ‘new avg’ weights provide the lowest average bias and lowest average spread, the PU 50 S2 optimised weights come a close second and provide a flatter bias response across the different energy bins. With 48b, the picture is much clearer. Above an energy of 2 GeV, the biases are small, but PU 50 S2 optimised weights bring the bias closer to 0 than the other three configurations. These PU 50 S2 optimised weights also provide the lowest average spread and perform consistently better across the high and low eta rings.

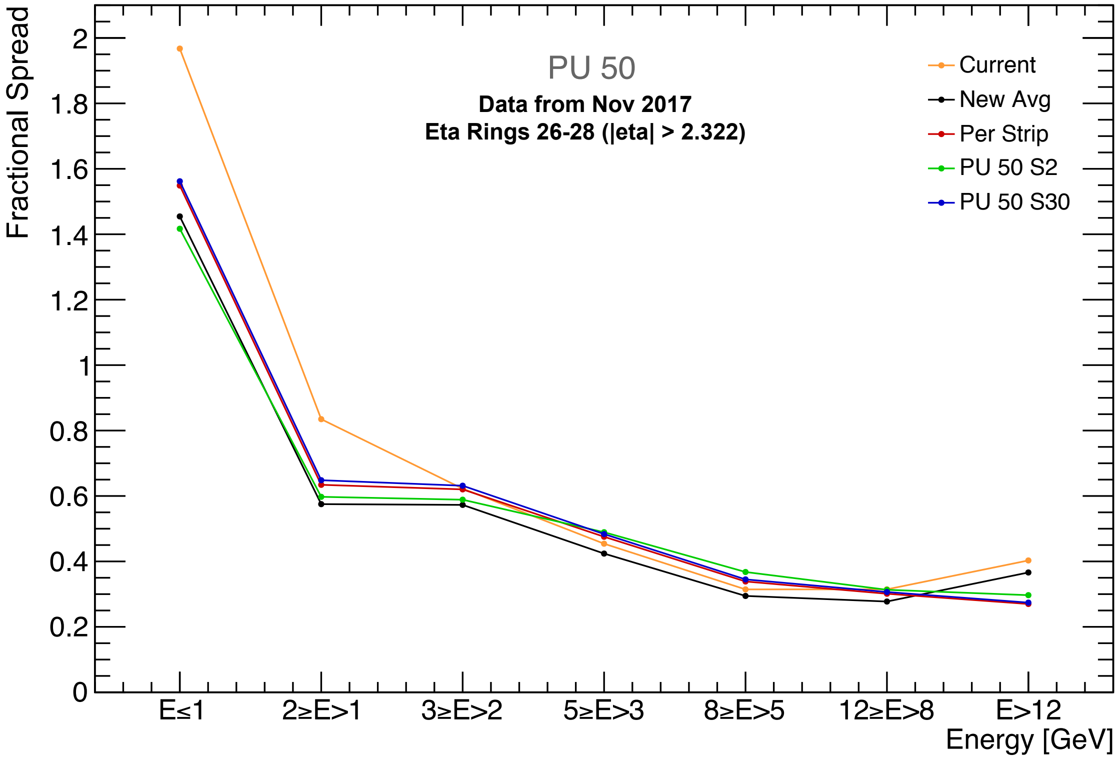

Figure 40: Spread against energy for 8b4e Run 306456 with PU 50 for EE eta rings 26 to 28.

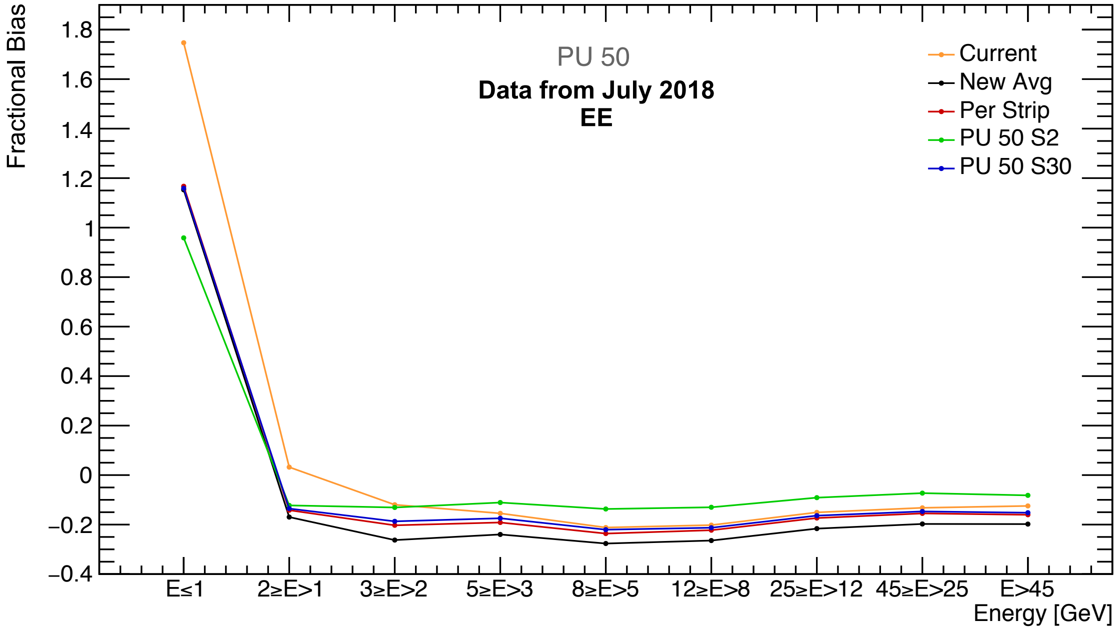

Figure 41: Bias against energy for 48b Run 320059 with PU 50 for all EE eta rings. Due to a larger number of events in the file, a greater number of energy bins were computed for 48b. The spreads are too large to plot here and the standard error on the means too small.

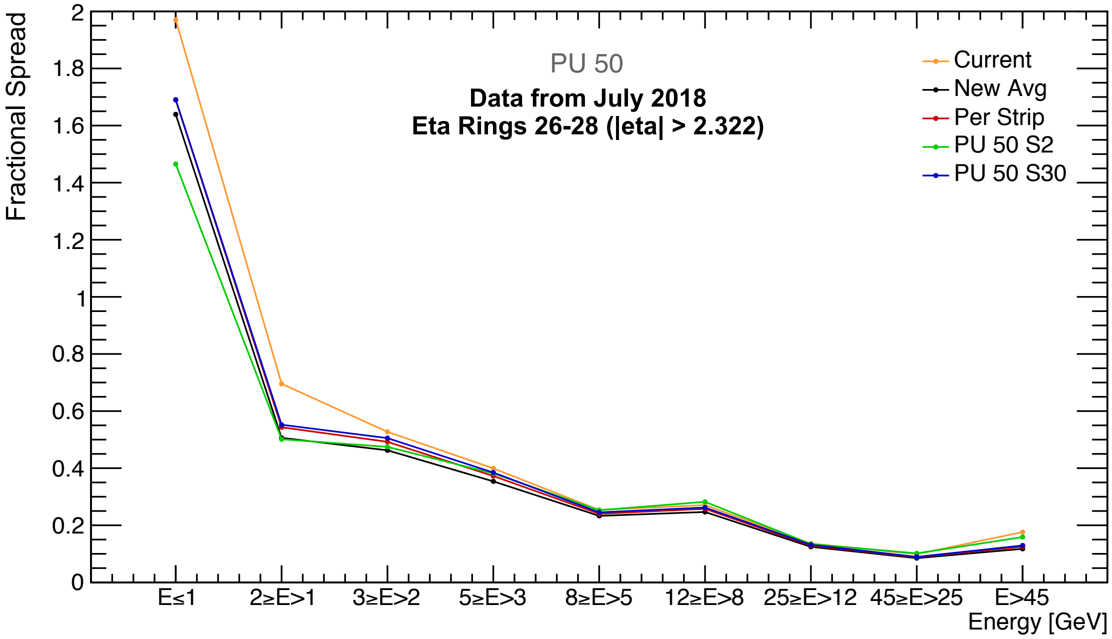

Figure 42: Spread against energy for 48b Run 320059 with PU 50 for EE eta rings 26 to 28.

| Data | Weights | Average Bias | Flatness | Average Spread |
|---|---|---|---|---|
| 8b4e PU 50<br>Whole EE | Current | 0.4193 | 0.6806 | 0.6943 |
| | New Avg | **0.1015** | 0.3693 | **0.5530** |
| | Per Strip | 0.1541 | 0.3634 | 0.5804 |
| | PU 50 S2 | 0.1551 | **0.3063** | 0.5601 |
| | PU 50 S30 | 0.1723 | 0.3613 | 0.5894 |
| 8b4e PU 50<br>Rings 18 - 21 | Current | -0.1729 | 0.0825 | 0.1173 |
| | New Avg | -0.2388 | 0.1122 | 0.1117 |
| | Per Strip | -0.1568 | 0.0814 | 0.1181 |
| | PU 50 S2 | **-0.0940** | 0.0859 | **0.0847** |
| | PU 50 S30 | -0.1564 | **0.0809** | 0.1179 |
| 8b4e PU 50<br>Rings 22 - 25 | Current | -0.0764 | 0.3977 | 0.2770 |
| | New Avg | -0.1730 | 0.3815 | 0.2407 |
| | Per Strip | -0.1111 | 0.3090 | 0.2499 |
| | PU 50 S2 | **-0.0672** | **0.2498** | **0.2311** |
| | PU 50 S30 | -0.1054 | 0.3085 | 0.2450 |
| 8b4e PU 50<br>Rings 26 - 28 | Current | 0.4740 | 0.7171 | 0.7015 |
| | New Avg | **0.1253** | 0.3691 | **0.5663** |
| | Per Strip | 0.1834 | 0.3714 | 0.5983 |
| | PU 50 S2 | 0.1850 | **0.3159** | 0.5814 |
| | PU 50 S30 | 0.2030 | 0.3689 | 0.6072 |
| 48b PU 50<br>Whole EE | Current | 0.0759 | 0.5945 | 0.4557 |
| | New Avg | -0.0747 | 0.4353 | 0.3782 |
| | Per Strip | -0.0352 | 0.4261 | 0.3930 |
| | PU 50 S2 | **0.0090** | **0.3364** | **0.3706** |
| | PU 50 S30 | -0.0260 | 0.4198 | 0.3965 |
| 48b PU 50<br>Rings 18 - 21 | Current | -0.0094 | 0.4352 | 0.3309 |
| | New Avg | -0.0763 | 0.4383 | 0.3140 |
| | Per Strip | -0.0527 | 0.3451 | 0.2992 |
| | PU 50 S2 | **-0.0370** | **0.3047** | **0.2867** |
| | PU 50 S30 | -0.0536 | 0.3238 | 0.2921 |
| 48b PU 50<br>Rings 22 - 25 | Current | -0.0890 | 0.4001 | 0.2772 |
| | New Avg | -0.1530 | 0.3895 | 0.2563 |
| | Per Strip | -0.1187 | 0.3895 | 0.2563 |
| | PU 50 S2 | **-0.0769** | **0.3083** | **0.2492** |
| | PU 50 S30 | -0.1150 | 0.3629 | 0.2606 |
| 48b PU 50<br>Rings 26 - 28 | Current | 0.1313 | 0.6428 | 0.5031 |
| | New Avg | -0.0531 | 0.4436 | 0.4187 |
| | Per Strip | -0.0124 | 0.4479 | 0.4375 |
| | PU 50 S2 | 0.0536 | **0.3423** | **0.4168** |
| | PU 50 S30 | **0.0008** | 0.4427 | 0.4434 |

Table 6: Results for bias against energy for the different datasets and weight configurations. Numbers in bold are the lowest in the column and show the weight configuration that performs best for that metric.

# 8 Final Conclusions

Various studies have been conducted to thoroughly investigate the energy reconstruction performance of the weights used in the ECAL trigger primitive energy reconstruction algorithm. The current weights, which have been used since CMS started taking data, have been shown to be no longer optimal. With the current weights, large biases and spreads are present in the reconstructed energy of CMS data. These large biases are predominantly in the innermost eta endcap rings, which have been damaged the most by the harsh LHC radiation. It has been shown that with the current weights, there is a large bunch position dependence of the energy bias in both the 8b4e and 48b filling schemes, although in 48b there is a central region of stability with lower bias there is also a large positive bias in the first few positions. Furthermore, low energy events in 8b4e, with energies less than 3 GeV, have large reconstruction biases associated with them. In 48b, events with an energy of 1 GeV or less have a large bias.

Updated weights of various granularities were computed from ECAL pulse shapes extracted from 2018 data, and the performance was compared to the current weights. An amplitude reconstruction bias study was carried out on pure pulse shapes, in the absence of PU, with these different granularity weights. A huge improvement was realised by increasing the granularity of the weights. Per strip weights effectively removed the bias and significantly reduced the spread. When applied to CMS data in the presence of PU however, these significant improvements were much less evident, although still present. Updated weights performed better than the current weights in all cases, especially in the innermost eta rings and at low energy, reducing the dependence of the bias on eta ring, bunch position and energy scale, but the difference between the different granularities was small. Clearly, PU has a large effect on the energy reconstruction performance of the weights.

PU optimised weights were computed from a PU MC simulation, and the measured bias against eta ring, bunch position and energy were plotted for all the weight configurations, for both 8b4e and 48b bunch filling schemes respectively. PU optimised weights reduced the average spread across the eta rings and the positions within the bunch trains most successfully, for both filling schemes and PU levels. In the majority of the eta regions, PU optimised weights also reduced the average spread across the different energy scales the most. Reducing the spread in the energy reconstruction bias in almost all of the studies carried out here, which, unlike an eta-dependent bias, cannot be corrected for with a simple calibration, represents a real performance improvement, which will result in more accurate energy measurements of physics objects by the ECAL trigger and therefore more recorded physics.

The effect of the LHC filling scheme on the energy reconstruction of the weights has been studied. For the same PU level, the biases and spreads in the higher eta rings with the 8b4e filling scheme are significantly larger than with 48b. In 8b4e, the largest biases come from the second bunch position, causing the majority of generated TPs to originate from this bunch position. Furthermore, the biases present with 8b4e are larger at every energy scale investigated than with 48b. Despite this, updated weights have been shown to significantly improve the performance in 8b4e and by updating the weights, the problems associated with the 8b4e filling scheme can be significantly reduced. PU optimised weights were very effective at improving the performance in 48b, whereas 8b4e was more changeable, although in every case changing from the current weights to an updated weight configuration yielded an improvement. For a potentially mixed bunch filling scheme containing both 8b4e and 48b currently being considered for LHC Run 3, PU optimised weights provide a good solution. In both filling schemes, PU optimised weights were more effective at reducing the average spread at higher PU than at lower PU, suggesting that at PU levels higher than investigated here, PU optimised weights will be more effective still.

Overall, it is clear that the current weights no longer reconstruct the energy of events accurately and perform particularly poorly with low energy TPs in the innermost rings of the ECAL endcaps. The current weights should be updated to suit current detector conditions. Although changing the weights to a new average set would be simple, the advantages of an increased weight granularity have been shown. Furthermore, PU optimised weights have been seen to most effectively reduce the average spreads present in each eta ring, bunch position and energy range. More accurate energy reconstruction, especially at high PU, reduces the number of unnecessary triggers from events with overestimated energy, and results in a lowered energy threshold, and ultimately more physics events being recorded for use in physics analyses. As the PU level at the LHC increases, the use of PU optimised weights will become even more vital for accurate energy reconstruction within the ECAL.

# 9 Future Work

## 9.1 Re-emulation of L1 Physics Objects

Throughout this project, the re-emulation of TPs has been the main focus, so that biases in energy reconstruction could be studied. It would also be valuable to re-emulate the L1 physics objects, such as electrons, photons, missing transverse energy and jets, so that the efficiencies and rates of the different physics triggers could be investigated. Any update to the weights or increased weight granularity should not negatively impact the triggers, and the rates must remain constant or be reduced and a high trigger efficiency must be maintained. This work will be carried out by the CMS L1 Trigger group using the weights identified in this study.

## 9.2 Filling Scheme Optimised Weights

It would be very interesting to compute PU optimised weights, optimised for the 48b filling scheme and then use them on 8b4e data, and vice versa. Investigating the biases present when the weights are mismatched with the filling schemes would provide information into how the weights would perform on a mixed filling scheme. In reality, the weights cannot be changed during an LHC Fill, so the weights would have to work well for the 48b and 8b4e filling schemes. Some research into this area would be valuable when deciding on the proportion of each filling scheme to have in the mixed scheme being considered for LHC Run 3.

## 9.3 Validation of PU Monte Carlo Simulation

Using the results presented in section 7, the PU MC Simulation used to derive the PU optimised weights can be validated. By producing the same plots as shown here but with the simulation, it should be possible to verify the simulation is reproducing the behaviour of the PU and detector correctly. Once successfully verified, the simulation will then be used to investigate other weight configurations, to evaluate their possible benefits.

## 9.4 Additional Weights

There exists the possibility that a sixth weight could be added, located before the existing five, which could further subtract any out-of-time PU contribution. When the weights were first derived at the start of LHC running, it was decided that additional weights, beyond the five, would give no extra benefit. However, the crystal pulse shapes have changed significantly since then and PU has increased substantially. The PU MC simulation will be expanded to allow for a sixth weight and will be used to investigate the potential performance improvements. If significant, this possibility will be explored in the emulator and on real hardware, in collaboration with software and hardware specialists. There is a further option to add a second set of weights for each strip, which would interact with the first to reduce the contribution from out-of-time signals, which may significantly improve the performance of the TP algorithm. Again, the PU MC simulation will first be used to motivate this, as this development would represent significant changes to the current algorithm.

## 9.5 Hardware Tests

There exists a test setup at CERN, with ECAL front-end electronics, that can be used for hardware and electronics testing. There is the possibility to inject a pulse shape into the electronics with different weight configurations and measure the TP response. This could be used to confirm changing to more granular weights doesn't increase the electronics configuration time. Furthermore, the changes mentioned above, such as a sixth weight or a second set of weights could be loaded into the electronics and tested. These kind of tests will be used as a proof of concept and functionality before significant changes to the L1 Trigger algorithms and software are made.

# References

[1] CERN. “About CMS and the LHC”. URL: `https://cms.cern/detector`. (accessed: 18.11.18).

[2] The CMS Collaboration. “The CMS experiment at the CERN LHC”. In: *Journal of Instrumentation* 3.S08004 (2008). URL: `http://iopscience.iop.org/article/10.1088/1748-0221/3/08/S08004/pdf`.

[3] The CMS Collaboration. “Observation of a new boson at a mass of 125 GeV with the CMS experiment at the LHC”. In: *Physics Letters B* 716.1 (2012), pp. 30–61. URL: `https://www.sciencedirect.com/science/article/pii/S0370269312008581`.

[4] The CMS Collaboration. “Description and performance of track and primary-vertex reconstruction with the CMS tracker”. In: *Journal of Instrumentation* 9.10 (2014), P10009. URL: `https://arxiv.org/pdf/1405.6569.pdf`.

[5] The CMS Collaboration. “The Hadron Calorimeter Technical Design Report”. In: *CERN Document* (1997). URL: `https://cdsweb.cern.ch/record/357153/files/CMS_HCAL_TDR.pdf`.

[6] The CMS Collaboration. “The Compact Muon Solenoid Technical Design Report”. In: *CERN Document* (1997). URL: `http://cds.cern.ch/record/343814/files/LHCC-97-032.pdf?version=1`.

[7] W.Smith. “Calorimeter Trigger Algorithms”. URL: `https://www.hep.wisc.edu/wsmith/cms/calgeo/`. (accessed: 15.1.19).

[8] A.Benaglia. “The CMS ECAL performance with examples”. In: *Journal of Instrumentation* 9 (2008), p. C02008. URL: `http://iopscience.iop.org/article/10.1088/1748-0221/9/02/C02008/pdf`.

[9] The CMS Collaboration. “The Electromagnetic Calorimeter Technical Design Report”. In: *CERN Document* (1997). URL: `https://cds.cern.ch/record/349375/files/ECAL_TDR.pdf`.

[10] CERN. “Triggering and Data Acquisition”. URL: `http://cms.web.cern.ch/news/triggering-and-data-acquisition`. (accessed: 2.12.18).

[11] P.Paganini. “ECAL Trigger Primitives and Selective Readout”. (accessed: 15.1.2019). 2008. URL: `https://indico.cern.ch/event/32151/contributions/745120/attachments/621156/854698/Paganini080417.pdf`.

[12] The CMS Collaboration. “Technical Design Report, Volume 1: The Trigger Systems”. In: *CERN Document* (2000). URL: `http://cmsdoc.cern.ch/cms/TDR/TRIGGER-public/CMSTrigTDR.pdf`.

[13] The CMS Collaboration. “The Trigger System”. In: *Journal of Instrumentation* 12.01 (2017), P01020. DOI: `https://arxiv.org/pdf/1609.02366.pdf`.

[14] M.Hansen. “CMS ECAL FENIX ASIC design methodology”. In: *CERN Record* (2005). URL: `https://cds.cern.ch/record/814323/files/p362.pdf`.

[15] P.Busson. “Digital Filtering for ECAL Trigger Primitives Generator”. In: *CERN CMS Note* 1999/020 (1999). URL: `http://inspirehep.net/record/876401/files/note99_020.pdf?version=2`.

[16] P.Paganini and I.van Vulpen. “Pulse amplitude reconstruction in the CMS ECAL using the weights method”. In: *CERN CMS Note* (2004). URL: `http://cds.cern.ch/record/801816/files/note04_025.pdf`.

[17] The CMS Collaboration. “Reconstruction of the signal amplitude of the CMS electromagnetic calorimeter”. In: *The European Physical Journal C - Particles and Fields* 46.1 (2006), pp. 23–35. URL: `https://link.springer.com/article/10.1140%5C%2Fepjcd%5C%2Fs2006-02-002-x4`.

[18] J.Blaha. “Calibration and performance test of the Very-Front-End electronics for the CMS electromagnetic calorimeter”. PhD thesis. Université Claude Bernard - Lyon, 2008.

[19] P.Lecoq et al. “Lead Tungstate Crystals for LHC EM-Calorimetry”. In: *CERN Document* (1994). URL: `http://cds.cern.ch/record/279798/files/ppe-94-225.pdf`.

[20] ECAL DPG. “Relative response to laser light”. URL: `https://twiki.cern.ch/twiki/pub//CMS/ECAL13TeVPage2019/histories_2011-2012-2015-2016-2017-2018_190208.png`. (accessed: 26.4.19).

[21] M.Lucchini. “EE pulse shape evolution as a function of Laser Correction”. (accessed: 15.1.2019). 2012. URL: `https://indico.cern.ch/event/211477/contributions/1506567/subcontributions/135923/attachments/331420/462210/ECAL_pulseshape.pdf`.

[22] G.Soyez. “Pileup mitigation at the LHC”. PhD thesis. Institut de Physique Theorique - CEA Saclay, 2018.

[23] A.Massironi. “Precision electromagnetic calorimetry at the energy frontier: CMS ECAL at LHC Run 2”. In: *Proceedings, Meeting of the APS Division of Particles and Fields (DPF 2015): Ann Arbor, Michigan, USA, 4-8 Aug 2015*. 2015. arXiv: `1510.02745 [physics.ins-det]`.

[24] M.Ferro-Luzzi W.Herr and T.Pieloni. “LHC bunch filling schemes for commissioning and initial luminosity optimization”. In: *CERN Project Note* 415 (2008). URL: `http://cds.cern.ch/record/1114612/files/LHC-PROJECT-NOTE-415.pdf`.

[25] A.Zabi and A.Brinkerhoff. “Effect of ECAL and HCAL conditions on L1T jets and MET”. (accessed: 26.4.2019). 2017. URL: `https://indico.cern.ch/event/674023/contributions/2805549/attachments/1573395/2483478/2017_12_11_L1T_JetMET_ECAL_HCAL.pdf`.

[26] M.Zarucki. “L1 Trigger Menu 2018 Performance and Development Plans for Run 3”. (accessed: 26.4.2019). 2019. URL: `https://indico.cern.ch/event/791517/contributions/3341732/attachments/1819684/2975695/L1Menu_Run3Developments_Zarucki_AlgorithmsWorkshopMadrid_28-03-2019.pdf`.

[27] D.Petyt. “Optimising the performance of the CMS ECAL to measure Higgs properties during Phase 1 and Phase 2 of the LHC”. (accessed: 26.4.2019). 2018. URL: `https://indico.cern.ch/event/732102/contributions/3187732/attachments/1761593/2858438/petyt_hc_2018.pdf`.

[28] A.Tishelman-Charny. “Online ECAL Reconstruction with Simulated Time Shifts”. (accessed: 3.5.2019). 2018. URL: `https://indico.cern.ch/event/760190/contributions/3155082/attachments/1723249/2782821/Weights_Studies_Update_26_September.pdf`.

[29] D.Valsecchi. “PU optimized weights for ECAL TP generation”. (accessed: 3.5.2019). 2019. URL: `https://indico.cern.ch/event/817480/contributions/3412893/attachments/1837763/3011641/ECAL_Trigger_meeting_2019_05_02_-_PU_optimized_weights_summary.pdf`.

[30] D.Valsecchi. “TPG weights optimization including the effect of the PU”. (accessed: 26.4.2019). 2019. URL: `https://indico.cern.ch/event/801425/contributions/3332627/attachments/1803201/2941765/DPG_27_02_2019_TPG_optimization_with_PU_Davide_Valsecchi.pdf`.

# A Code Used for Figures and Tables

The following programs were used to generate the figures and data in the tables in this thesis. The code is available at: https://gitlab.cern.ch/wrsmith/tpg-weights and https://drive.google.com/open?id=1yVPg_Jtgwv8xMQdeq_-Hrf3iwDjl6BPK. For any questions, I can be contacted on wrsmith97@gmail.com.

- Figures 15, 16, 17: SWAN_projects/Weight_bias/weight_bias_perEE_EB_current.ipynb
- Figure 18: macros/tpgplot_weights.C
- Figure 19: macros/tpgplot_1d_oldWeights_for_report.C
- Figure 20, 21: SWAN_projects/Weight_bias/weight_bias_perEE_EB.ipynb
- Figure 22: SWAN_projects/TP-eRec/profile_plots_comparison_tp_minus_erec_newAVG_and_current.ipynb
- Figure 23: macros/tpgplots_1d_weights.C
- Figure 24: SWAN_projects/Weight_change_map/rootweightmap_perSTRIP.ipynb
- Figure 27: SWAN_projects/Weight_bias/weights_bias_compare_1dhist.ipynb
- Figure 28: SWAN_projects/TP-eRec/Compare/TP-eRec_320065_all_granularities.ipynb
- Figure 29: SWAN_projects/TP-eRec/Compare/1D_plots_comparison_tp_minus_erec_FULL_smallerbins.ipynb
- Figures 33, 34: SWAN_projects/Analysis/Bias/2017/Bias_vs_etaRing_306456_PU50_S2.ipynb
- Figures 35, 36: SWAN_projects/Analysis/Bias/Bias_vs_etaRing_320059_PU50_S2.ipynb
- Figure 37: SWAN_projects/Analysis/Bias/2017/Bias_vs_bx_position_306456_PU50_S2.ipynb
- Figure 38: SWAN_projects/Analysis/Bias/Bias_vs_bx_position_320059_PU50_S2.ipynb
- Figure 39: SWAN_projects/Analysis/Et_bins/Bias_vs_Et_306456_all_rings.ipynb
- Figure 40: SWAN_projects/Analysis/Et_bins/Bias_vs_Et_306456_26_to28.ipynb
- Figure 41: SWAN_projects/Analysis/Et_bins/Bias_vs_Et_320059_all_rings.ipynb
- Figure 42: SWAN_projects/Analysis/Et_bins/Bias_vs_Et_320059_all_26_to28.ipynb
- Table 4:

  SWAN_projects/Analysis/Bias/2017/Bias_vs_etaRing_306459_PU30_S2.ipynb
  SWAN_projects/Analysis/Bias/2017/Bias_vs_etaRing_306456_PU50_S2.ipynb
  SWAN_projects/Analysis/Bias/Bias_vs_etaRing_320059_PU50_S2.ipynb
  SWAN_projects/Analysis/Bias/Bias_vs_etaRing_320065_PU30_S2.ipynb
- Table 5:

  SWAN_projects/Analysis/Bias/2017/Bias_vs_bx_position_306459_PU30_S2.ipynb
  SWAN_projects/Analysis/Bias/2017/Bias_vs_bx_position_306456_PU50_S2.ipynb
  SWAN_projects/Analysis/Bias/Bias_vs_bx_position_320065_PU30_S2.ipynb
  SWAN_projects/Analysis/Bias/Bias_vs_bx_position_320059_PU50_S2.ipynb

- Table 6:

  SWAN_projects/Analysis/Et_bins/Bias_vs_Et_306456_all_rings.ipynb
  SWAN_projects/Analysis/Et_bins/Bias_vs_Et_306456_18_to21.ipynb
  SWAN_projects/Analysis/Et_bins/Bias_vs_Et_306456_22_to25.ipynb
  SWAN_projects/Analysis/Et_bins/Bias_vs_Et_306456_26_to28.ipynb
  SWAN_projects/Analysis/Et_bins/Bias_vs_Et_320059_all_rings.ipynb
  SWAN_projects/Analysis/Et_bins/Bias_vs_Et_320059_18_to21.ipynb
  SWAN_projects/Analysis/Et_bins/Bias_vs_Et_320059_22_to25.ipynb
  SWAN_projects/Analysis/Et_bins/Bias_vs_Et_320059_26_to28.ipynb